CERN Summer Student Lectures. Detectors. A write-up.

O. Ullaland
PH Department
European Organization for Nuclear Research
CH 1211 Genève 23
e-mail: olav.ullaland@cern.ch

Abstract

Any device that is to detect a particle must interact with it in some way. If the particle is to pass through the detection system essentially undeviated, this interaction must be a soft electromagnetic one. There is another type of detector system that will measure the energy and the position of the particle by total absorption in these devices.

1 Introduction

This write-up of the Detector lectures which was given in the context of the CERN Summer Student lecture series, will give a general, although somewhat compressed, introduction to particle interaction with matter and magnetic fields. Tracking detectors and calorimeters will also be covered as well as particle identification systems. This write-up does not aim to be a complete stand-alone discussion of particle interactions nor to give an exhaustive coverage of experimental techniques in physics. This can be found in a number of excellent text books. Some of them are listed in reference [1]. The mathematical formalism that is used in this write-up is based on reference [2] and it is assumed that the reader is familiar with the formalism of electrodynamics.

The note will start out with a short review of particle interaction with fields and then we will discuss particle detection. At the end some common composite detection systems will be described. Only minor changes have been introduced since the 2004 edition.

2 Particle Interaction with Fields

2.1 From Rutherford to Bethe-Bloch

The angular deflection of a particle with mass m_1, charge eZ_1 and velocity v_0 on a target particle of mass m_2 and charge eZ_2 can be written in the centre of mass coordinate system

$$\tan\frac{\Theta_{CM}}{2} = \frac{K}{v_0^2 b} \qquad \text{where} \qquad K = \frac{e^2 Z_1 Z_2}{4\pi\varepsilon_0 m_r} \qquad \text{and} \qquad m_r = \frac{m_1 m_2}{m_1 + m_2}$$

and b is the impact parameter as defined in Fig. 1. This is the classic nonrelativistic representation of Rutherford scattering. By integrating over the impact parameter b

$$\frac{dN}{d\Omega} = \frac{N_0}{256\pi^2\varepsilon_0^2}[nt]e^4 Z_1^2 Z_2^2 \frac{1}{(\frac{1}{2}m_1 v_0^2)^2}\frac{1}{\sin^4\frac{\Theta_{CM}}{2}} \qquad \text{where}$$

N_0	number of beam particles
n	target material in atoms/volume
t	target thickness

As there is a screening by the electric field of the atom, there is a minimum scattering angle $\overline{\Theta_{min}}$ which is approximately inversely proportional to the momentum of the particle. For a single scattering, the mean scattering angle is thereby given as

$$\overline{\Theta^2} \approx 2\Theta_{min}^2 \ln\frac{\Theta_{max}}{\Theta_{min}} \qquad \text{or for N multiple scatterings} \qquad \overline{\Theta^2_{\mathrm{MS}}} \approx \frac{N_0\rho dx}{A}2\pi\left\{\frac{2Z\alpha}{p\beta c}\right\}^2[\ln()]$$

The slowly varying logarithmic term will be ignored. Multiple Coulomb scattering can be treated as classic Rutherford scattering. If the energy of the particle is above the ionisation energy, I, of the material, an electron escapes the atom. If the energy is below I, no energy is transferred. The mean excitation energy is plotted in Fig. 2 where $I/Z = 10 \pm 1$ eV for $Z > 18$. The nonrelativistic energy loss for a particle in matter can thereby be written as

$$\frac{dE}{dx} = \frac{NZ_1^2e^4}{8\pi\varepsilon_0^2 m_e v_0^2}\sum_{i=Z`}^{Z}\ln\frac{2m_r^2v_0^2}{m_e I_i}$$

If we ignore the slowly varying logarithmic term, the range, R, of a particle in matter would be proportional to the squared of the ratio of the kinetic energy divided by the Z of the material. We can compare this to the current wisdom of the Bethe-Bloch formula [3] plotted in Fig. 3

$$\frac{dE}{dx} = Kz^2\frac{Z}{A}\frac{1}{\beta^2}\left\{\frac{1}{2}\ln\frac{2m_e c^2\beta^2\gamma^2 T_{max}}{I^2} - \beta^2 - \frac{\delta}{2}\right\}$$

$$\frac{K}{A} = \frac{4\pi N_A r_e^2 m_e c^2}{A} = 0.307075 \text{ MeVg}^{-1}\text{cm}^2 \text{ for A=1 g/mol} \quad \text{and } T_{max} = \frac{2m_e c^2\beta^2\gamma^2}{1 + 2\gamma\frac{m_e}{M} + (\frac{m_e}{M})^2}$$

By comparing the relativistic and the nonrelativistic computation of the range, Fig. 4, we see that the range is approximately proportional to the energy square at low energy and proportional to the energy where *dE/dx* is about constant, on the Fermi plateaux. Further discussion can be found in [4].

2.2 Bremsstrahlung, photon pair production and radiation length

The Feynman diagrams for Bremsstrahlung and photon pair production are given in Fig. 5. Let us first consider Bremsstrahlung as a nonrelativistic radiative process. Let b be the impact parameter. The peak electric field is proportional to e/b^2 and the characteristic frequency $\omega_c \propto \Delta t^{-1} \propto \frac{v}{2b}$. This process is described by

$$dU = \int du = \iint\left(\frac{dE}{d\omega}\right)^2 d\omega \cdot 2\pi b db = \int\frac{dU}{d\omega}d\omega \qquad \Rightarrow \qquad \frac{dU}{d\omega} = 4\frac{\alpha}{\beta^2}[\ln()]$$

The differential cross section for Bremsstrahlung can be written as

$$\frac{d\sigma_B}{d\omega} \approx Z^2 \frac{dN_\gamma}{d\omega}\sigma_T \qquad N_\gamma : \text{photon density} \qquad \sigma_T : \text{Thomson cross section}$$

$$\Downarrow \qquad \frac{dN_\gamma(\omega)}{d\omega} \approx \frac{2\alpha}{\pi}\frac{1}{\beta^2}\frac{1}{\omega}[\ln()] \qquad \sigma_T = \frac{8\pi}{3}(\alpha\lambda\!\!\!^{-})^2$$

$$\sigma_B \sim 0.58 \text{ mb } \cdot Z^2$$

By comparing the Feynman diagrams in Fig. 5, we would assume that the cross section for pair production would be very similar to that of Bremsstrahlung, $\sigma_{\text{pair}} = \frac{7}{9}\sigma_B \approx 0.45$ mb $\cdot Z^2$ The radiative energy loss by Bremsstrahlung can be written as

$$dE \approx \int_0^E \hbar\omega \frac{N_0 \rho dx}{A}\frac{d\sigma_B}{d\omega}d\omega \quad \text{Define } X_0 \equiv \text{Radiative Mean Path} \quad \frac{1}{X_0} \equiv \frac{1}{E}\frac{dE}{\rho dx}$$
$$\equiv \text{Radiation Length}$$

and

$$X_0^{-1} = \frac{16}{3}\frac{N_0}{A}Z^2\alpha(\alpha\lambda\!\!\!^{-})^2[\ln()] \propto \frac{Z^2}{A}$$

Radiation length as function of Z is plotted in Fig. 6. The multiple scattering angle, $\overline{\Theta^2_{MS}}$, can be expressed as function of the radiation length

$$\sqrt{\overline{\Theta^2_{MS}}} = \frac{E_S}{p\beta}\sqrt{\frac{dx}{X_0}} = \frac{E_S}{p\beta}\sqrt{t},\ t \text{ is the thickness of the material expressed in radiation lengths.}$$

We have here introduced the characteristic energy, $E_S \equiv m_e c^2\sqrt{\frac{4\pi}{\alpha}} = 21.205$ MeV.

When we later will discuss calorimeters as particle detectors, we will expand the initiating particle in ionisation. The classic way to do this is by using the Rossi II approximation to electromagnetic shower development [5].

1. Electrons lose a constant amount of energy, ϵ, for each radiation length, X_0.

2. Radiation and pair production at all energies are described by the asymptotic formulae.

We will define the critical energy, E_C, as the energy where Bremsstrahlung is equal to Ionisation. A high energy electron can lose energy by emitting gamma radiation if it is deflected. Below this critical energy of the material, the electron no longer loses energy in this way; it simply ionises atoms or is scattered. The fractional energy loss is plotted in Fig. 7 together with the critical energy as a function of Z. The photon total cross section is plotted in Fig. 8.

2.3 Nuclear interaction length

The mean free path of a particle in a medium is a measure of its probability to undergo interactions of a given kind. It is related to the cross section corresponding to this type of interaction by the formula

$$\sigma\lambda = \frac{\Omega}{N} = \frac{A}{N_A\rho}$$

Where σ is the cross section [cm^2], λ the mean free path [cm], Ω the volume of interaction, N the number of target particles in Ω, A the atomic weight [g/mol], N_A is Avogadro's number and ρ is the density [g/cm^3]. The relevant cross section is $\sigma_{\text{total}} - \sigma_{\text{elastic}} - \sigma_{\text{diffractive}}$. For hadronic interactions, the interesting quantity is the nuclear interaction length, λ_I. It is nearly energy independent and approximately proportional to $A^{1/3}$ as shown in Fig. 9.

2.4 Cherenkov radiation

The density effect in the energy loss, Fig. 3, is intimately connected to the coherent response of a medium to the passage of a relativistic particle. This causes the emission of Cherenkov radiation. Let us consider charged particle interaction with matter as described in Fig. 10. If $\omega \ll \gamma m$ and $k \ll \beta\gamma m$, then

$$\cos\Theta_C = \frac{1}{\beta\sqrt{\varepsilon}} \quad \Longleftarrow \begin{cases} \omega = \vec{\beta}\cdot\vec{k} & \text{from conservation of energy and momentum} \\ \omega^2 - \frac{k^2}{\varepsilon} = 0 & \text{from dispersion relation} \end{cases}$$

We have here considered the electric permeability, ε, as a real number. ε for argon is plotted in Fig. 11. The refractive index of argon at NTP, can in the Sellmeier approximation be written as $(n-1)10^6 = 0.05139 \cdot [16.88^2 - E^2]^{-1}$, where E is the photon energy in eV. We observe that the refractive index is undefined at the value where the electric permeability goes from above 1 to below 1 and where the imaginary part becomes important. This is at the plasma frequency, ω_0, for the material. The square of the plasma frequency is approximately proportional to the electron density in the material. By calculating the electromagnetic energy flow in a cylinder of radius a around the track of the particle [2], we get after some steps

$$\left(\frac{dE}{dx}\right)_{b>a} \quad \underset{|\lambda a|\gg 1}{\longrightarrow} \quad Re\left[\int_0^\infty \frac{z^2e^2}{c^2}\left(-i\sqrt{\frac{\lambda^*}{\lambda}}\right)\omega\left(1-\frac{1}{\beta^2\varepsilon(\omega)}\right)e^{-(\lambda+\lambda^*)a}d\omega\right]$$

where a is in the order of atomic dimension, b is the impact parameter and

$$\lambda^2 = \frac{\omega^2}{v^2} - \frac{\omega^2}{c^2}\varepsilon(\omega) = \frac{\omega^2}{v^2}\left[1-\beta^2\varepsilon(\omega)\right]$$

If λ has a positive real part, the integrand will vanish rapidly and all energy is deposited near the track. If λ is purely imaginary, the integrand is independent of a and some energy will escape as radiation. For λ to be purely imaginary, $\beta^2\varepsilon > 1$, which is the Cherenkov condition. We also see that $\frac{dE}{dx} \propto \sin^2\Theta_C$. We will come back to detectors for Cherenkov radiation in section 4.1.

2.5 Transition radiation

There is another type of radiation, transition radiation [8], that is emitted when a charged particle passes suddenly from one medium to another. If $\varepsilon < 1$ no real photon can be emitted for an infinitely long radiator. Due to diffraction broadening, there is a sub-threshold emission of real photons in thin radiators.

$$\text{If} \quad \omega \gg \omega_{i0} \qquad \frac{d^2S_0}{d\Theta d\omega} = \frac{2\alpha\hbar\Theta^3}{\pi\omega}\left[\frac{1}{a_1}-\frac{1}{a_2}\right]^2 \qquad \text{where} \quad a_i = \frac{1}{\gamma^2} + \Theta^2 + \frac{\omega_{0i}^2}{\omega^2}$$

If $\omega_2 \gg \omega_1$ then the angle of maximum radiation, $\Theta_{max} \approx \gamma^{-1}$, and the total radiated power $S(\text{eV}) \approx 10^{-2}\cdot\gamma$. The classic way to increase the number of produced photons from transition radiation is to construct a periodic radiator as in Fig. 12. Further discussion can be found in [8]. We will come back to detectors for transition radiation in section 4.1.

2.6 Magnetic fields and momentum measurements

The classic Lorentz force equation, $\vec{F} = q\cdot\vec{E} + q\cdot\vec{v}\times\vec{B}$, describes the force experienced by a charge q in an environment with an electric field strength, $\vec{E}$, and a magnetic flux density, $\vec{B}$. Magnet elements may be represented to a good approximation by a linear transformation matrix M operating on the displacement-divergence vectors (x, x') and (y, y'). The particle

motion is along z and the prime denotes d/dz and $|M| = 1$. Fig. 13 gives a representation of ideal dipole and quadrupole magnets. By using the Lorentz force equation and the nomenclature from Fig. 13, a rectangular bending magnet can then be represented by

$$\begin{bmatrix} x_2 \\ x_2' \end{bmatrix} = \begin{bmatrix} \frac{\cos\beta}{\cos\alpha} & R\sin(\alpha+\beta) \\ 0 & \frac{\cos\alpha}{\cos\beta} \end{bmatrix} \begin{bmatrix} x_1 \\ x_1' \end{bmatrix} \underset{\alpha=\beta=\frac{\phi}{2}}{\longrightarrow} \begin{bmatrix} x_2 \\ x_2' \end{bmatrix} = \begin{bmatrix} 1 & R\sin(\phi) \\ 0 & 1 \end{bmatrix} \begin{bmatrix} x_1 \\ x_1' \end{bmatrix}$$

and $\phi \cong 0.03BL/p$ with B in kG, L in m and p in GeV/c. With the same considerations, we can now write the transformation matrix for an ideal quadrupole magnet as described in Fig. 13. Different matrices will apply in the focusing and the defocusing plane.

$$M_{\text{focusing}} = \begin{bmatrix} \cos\omega d & \omega^{-1}\sin\omega d \\ -\omega\sin\omega d & \cos\omega d \end{bmatrix} \qquad M_{\text{defocusing}} = \begin{bmatrix} \cosh\omega d & \omega^{-1}\sinh\omega d \\ \omega\sinh\omega d & \cosh\omega d \end{bmatrix}$$

where d is the length of the element in m, $\omega^2 \cong 3\frac{k}{p}$ for k in kG/cm and p in GeV/c. In the same way as in optics, we can rewrite these matrices in a thin lens analogy. The effect of a thin lens is to change the divergence instantaneously without effecting the displacement. Each plane in a quadrupole corresponds to a thin lens of focal length f and a drift length s.

$$\begin{bmatrix} 1 & s \\ 0 & 1 \end{bmatrix} \begin{bmatrix} 1 & 0 \\ f^{-1} & 1 \end{bmatrix} \begin{bmatrix} 1 & s \\ 0 & 1 \end{bmatrix} = \begin{bmatrix} 1+sf^{-1} & s(2+sf^{-1}) \\ f^{-1} & 1+sf^{-1} \end{bmatrix}$$

The situation normally considered when using thin lens approximation is when $\omega d \to 0$. We then get $f^{-1} \to \pm\omega^2 d$ and $s \to 0.5d$. It can be verified that a quadrupole doublet can have a net focusing/defocusing effect on a particle beam. Further reading can be found in [9].

The momentum of the charged particle is usually calculated from the curvature in a magnetic field. Consider a particle trajectory in a magnetic field as described in Fig. 14. The momentum of the particle is given by [10]

$$p \cong \frac{q}{3}BR\sin\alpha \quad p \cong \frac{q}{3}\frac{BR_T}{\sin\alpha} \quad \underbrace{p \cong \frac{q}{3}B\left[\frac{C^2\sin\alpha}{2S} + \frac{S}{2\sin\alpha}\right]}_{\text{B uniform along trajectory}} \quad p \cong \frac{q}{3}\frac{\int B_T dl}{\Theta}$$

where B is the magnetic induction, R is the radius of curvature in trajectory space, α is the angle between the tangent to the trajectory and $\vec{B}$, C is the length of the chord and S the related sagitta. Θ is the bending angle. Subscript $_T$ indicates the projection onto a plane perpendicular to $\vec{B}$. A beam with momentum-analysed particles may consist of particles of different mass. A standard device for velocity separation is generally a parallel plate capacitor of length L along z. Consider a vertical, y, E field. The deflection and the divergence difference between two particles with mass m_1 and m_2 can be written like

$$\Delta y = -\frac{1}{2}kEL^2 \quad \text{and} \quad \Delta y' = -kEL \qquad \text{for} \quad k = \frac{e}{pc}\frac{\beta_1 - \beta_2}{\beta_1\beta_2}$$

At high momenta, $k \sim \left(m_2^2 - m_1^2\right)/2\,(pc)^3$.

2.7 Synchrotron radiation

It is well known that accelerated charges emit electromagnetic radiation. Deflection of ultra relativistic particles in magnetic fields leads to emission of radiation called synchrotron radiation.

Following reference [2], and after some manipulation of the 4-vector potential caused by a charge in motion, it can be shown that

$$\vec{B} = \left[\vec{n} \times \vec{E}\right]_{ret} \qquad \vec{E}\left(\vec{x},t\right) = \underbrace{e\left[\frac{\vec{n}-\vec{\beta}}{\gamma^2\left(1-\vec{\beta}\cdot\vec{n}\right)^3 R^2}\right]_{ret}}_{\text{Velocity field}} + \underbrace{\frac{e}{c}\left[\frac{\vec{n}\times\left[\left(\vec{n}-\vec{\beta}\right)\times\vec{\beta}'\right]}{\left[1-\vec{\beta}\cdot\vec{n}\right]R}\right]_{ret}}_{\text{Acceleration field}}$$

where $d\tau = dt/\gamma$, $\vec{n}$ is the unit vector in the direction of $\vec{x} - \vec{r}(\tau)$, $\vec{\beta} = \vec{\mathrm{v}}/\mathrm{c}$, $\vec{\beta}' = d\vec{\beta}/dt$ and $R = x_0 - r_0(\tau_0)$ as defined in Fig. 15. The subscript $_{ret}$ means that the quantity is to be evaluated at the retarded time τ_0. The velocity field is essentially a static field that falls off as R^2, whereas the acceleration field depends linearly on $\vec{\beta}'$ and is inversely proportional to R. The total energy loss is given by

$$\frac{dW}{dt} = \frac{2\mathrm{c}}{3}e^2\beta^4\gamma^4\frac{1}{r^2} \qquad \text{and the root mean square of the emission angle is} \quad \left[\overline{\Theta^2}\right]^{\frac{1}{2}} \cong \frac{1}{\gamma}$$

and is independent of the vector relationship between $\vec{\beta}$ and $\vec{\beta}'$. r is the bending radius of the charged particle. As $\beta\gamma = p/m$, synchrotron radiation is mainly observed with low-mass particles.

3 Particle Detection

3.1 Gaseous Detectors

Consider the simple detector geometry given in Fig. 16a. Let the metallic anode wire have a radius r_0 and the metallic cathode cylinder a radius R, $r_0 \ll R$. A minimum ionising particle will leave along the track in the gas, N_{total} ion pairs and free electrons. $N_{total} \approx 5 \cdot Z/\mathrm{cm}$ at NTP, where Z is the atomic number of the filling gas as given in Fig. 16b. The electric field next to the anode can be written as $E_0 = V_0 / \left[r_0 \ln\frac{R}{r_0}\right]$. V_0 is the voltage difference between the anode and the cathode. Let α^{-1} be the mean free path between each ionisation induced by the free electrons on the gas atoms as the electrons fall towards the anode. $\alpha = \alpha(E)$ and $E = E(r)$. α is generally known as the First Townsend coefficient. The total amount of electrons reaching the anode, the gas amplification constant, can then be written as

$$M = e^{\int_{r_0}^{r}\alpha(r)dr} \qquad \text{Korff approximation:} \quad \alpha = Ape^{-Bp/E} \quad \rightarrow M = \exp\left[\frac{A}{B}\frac{V_0}{\ln\frac{R}{r_0}}e^{\frac{Bpr_0\ln\frac{R}{r_0}}{V_0}}\right]$$

where p is the gas pressure and A and B are gas dependent constants, see Table 1. Fig. 17a shows an example of the characteristic energy for an electron as function of the electric field. Clearly the field has to be very high for the energy to be above the ionisation potential. A dramatic change can be observed in a gas mixture, Fig. 17b. This is the Penning effect. The metastable states are responsible for this effect. It allows to convert a greater fraction of the energy which was initially lost in excitation, into ion pairs, if the admixed gas component has a lower ionisation potential than the available energy of the excited state. The excited atoms of the principal gas are then able to transfer this energy in ionising collisions with molecules of the admixed component. It is thereby possible to have $\alpha \gg 0$ for reasonable electric fields and to begin the gas amplification process and to start the electron avalanche towards the anode. The main bulk of the electrons will be produced within a few anode diameters from the anode.

At the same time as the electrons are created, positively charged ions are created. The de-excitation of these ions will normally involve the emission of a photon. If the photon energy

is above the ionisation threshold for other molecules in the set-up, new free electrons will be created and thereby permanent discharges. Poly-atomic gases are therefore added to noble gases as quenchers. An example is shown in Fig. 18. The different operating regions for a chamber are shown in Fig. 19 for a heavily ionising α particle and for a β particle which is near minimum ionising.

There will also be effects due to the way the electrons are collected at the anode. The electric field of the chamber will be screened by the positive ions. The gas amplification will therefore change as the angle between the electric field and the ionising particle changes. The drift velocity and the diffusion of the electrons will change with the gases that are used in the chamber. A magnetic field will change the drift path of the electrons as well as the diffusion.

The schematics of a classic multiwire proportional chamber is shown in Fig. 20 together with the electric field configuration. The relationship between the voltage, the charge and the magnitude of the electric field can be written as

$$V_s(z) \underset{d\to 0}{\approx} \frac{2\pi l}{s} - \ln\left[4\sin^2\left(\frac{\pi x}{s}\right) + 4\sinh^2\left(\frac{\pi y}{s}\right)\right] \qquad \text{which gives} \qquad Q = \frac{V_0}{\frac{2\pi l}{s} - 2\ln\frac{\pi d}{s}}$$

$$\text{and} \qquad E_0 = \frac{sV_0}{\frac{\pi d}{2}\left[l - \frac{s}{\pi}\ln\frac{\pi d}{s}\right]}$$

The positive pulses that are induced by the positive ions onto the neighbouring anode wires are much greater than the negative pulses induced electrostatically. The net effect is therefore positive. The signal induced is mainly by the positive ions moving in the high electric field. Following reference [11] and assuming that all charges are created a distance λ from the anode, we can write

$$V_{electron} = -\frac{Q}{lCV_0}\int_{r_0}^{r_0+\lambda}\frac{dV}{dr}dr = -\frac{Q}{2\pi\varepsilon_0 l}\ln\frac{r_0+\lambda}{r_0}$$

$$V_{ion} = +\frac{Q}{lCV_0}\int_{r_0+\lambda}^{R}\frac{dV}{dr}dr = +\frac{Q}{2\pi\varepsilon_0 l}\ln\frac{R}{r_0+\lambda}$$

where lC is the total capacitance. As λ is in the order of a few μm, $V_{electron} \sim V_{ion}/100$.

The simple detector configurations that we have discussed above, can be readily understood. For a more complicated geometry, computer aided calculations will be necessary [13]. All derivative devices like the Drift Chamber (DC), the Time Projection Chamber (TPC), the MicroStrip Gas Chamber (MSGC), the Gas Electron Multiplier (GEM) or similar detectors, will adhere to the same principles as we have discussed above. Further reading can be found in [11] and [14]. Reference [12] gives a thorough discussion of electrons and ions in gases.

In the discussion of the Bethe-Bloch formula in page 2 and plotted in Fig. 3, the energy loss of a charged particle in matter is a function of the $\beta\gamma$ of the particle. We normally define it into four regions: the $1/\beta^2$ region, the minimum ionising region, the relativistic rise and the Fermi plateau region. As the total number of ions created in the gas is proportional to the energy lost by the charged particle, we can use the charge collected in the proportional chamber together with a measurement of the momentum of the particle as a measure for the energy of the particle. Thereby we can make a mass hypothesis for the particle. The measured charge has unfortunately large statistical fluctuations due to the primary ionisation process and the gas amplification process. In addition, there is the creation of δ electrons, knock-on energetic electrons which will travel far in a gas volume, that will add to the uncertainty of the measurement. The charge collected in a thin gas gap is well described by a Landau-like function [15]. It can be approximated to

$$\Psi(\lambda) = \sqrt{\frac{e^{-\left(\lambda+e^{-\lambda}\right)}}{2\pi}}$$

where $\lambda = R(E - E_p)$. E_p is the most probable energy loss and R is a detector specific constant. A histogram of the charge collected in a proportional chamber is given in Fig. 21a. To suppress large fluctuations, it is normal to take many samples along the track and to make a truncated mean measurement. That is, to ignore the x % highest and y % lowest measurements and take the mean of the remainder. This estimate will be near Gaussian distributed. An example of the result is shown in Fig. 21b.

3.2 Solid State Detectors

The resistivity of a material falls into one of three classes. The insulator with a volume resistivity between 10^9 and 10^{20} Ωcm, the semiconductor between 10^{-2} and 10^1 Ωcm and the conductor between 10^{-6} and 10^{-3} Ωcm. Each electron in a solid has a certain total energy which is made up from kinetic and potential energy. The complete energy axis can be divided into the forbidden bands, no electron can have these energies, and the allowed bands where there may be electrons. The band structure is shown in Fig. 22a. The distinction between an insulator and a semiconductor is one of degree rather than kind. The insulator has a band gap between the valence band and the conduction band of ≥ 3 eV, whereas this band gap is between 0.1 and 2.5 eV in a semiconductor. The density of states, $S(W)$, as function of the energy, W, is of course zero in the band gaps. For the lower edge of the conduction band

$$S(W) = \frac{4\pi}{h^3}(2m_e)^{\frac{3}{2}}(W - W_c)^{\frac{1}{2}}$$

and for the upper edge of the valence band

$$S(W) = \frac{4\pi}{h^3}(2m_h)^{\frac{3}{2}}(W_v - W)^{\frac{1}{2}}$$

where W_i is the energy at the edge of the band and m_i denotes the effective masses of carriers, holes or electrons, at the two band edges. The curves for $S(W)$ are to a first approximation parabolic. Let $P(W)$ describe the probability that a state at an energy W is occupied by an electron. These states will follow the Fermi-Dirac statistics and for a system in thermal equilibrium, we get

$$P(W) = \frac{1}{1 + e^{\frac{W - W_F}{\kappa T}}} \qquad \underset{\exp\left[\frac{W-W_F}{\kappa T}\right] \gg 1}{\longrightarrow} \qquad P(W) = e^{-\frac{W - W_F}{\kappa T}}$$

W_F is the Fermi level. It is defined as the energy where $P(W) = 1/2$. The number of electrons occupying states at different energies, is then given by $S(W) \cdot P(W)$. See Fig. 22b. By integrating this function from W_c, the lower edge of the conductance band, to W_t, the upper edge of the band, we get the number of electrons, n, in the conduction band. W_t is set equal to ∞ for ease of computation. The number of holes, p, in the valence band can be found in the same way by using $1 - P(W)$ instead of $P(W)$ and integrating from W_v at the top of the valence band. We then get for the Fermi level for a thermal equilibrium situation

$$W_F = \frac{W_c + W_v}{2} - \frac{\kappa T}{2} \ln \frac{p}{n} - \frac{3}{4} \kappa T \ln \frac{m_e}{m_h}$$

When $p \neq n$, then the Fermi level shifts towards the band with the majority carrier. In the case when p and n are controlled by an external device, the system may be far from equilibrium and $pn \neq n^2$.

One way to move the Fermi level is to dope the semiconductor. There are two kinds of dopant, donors and acceptors. A list is given in Table 2. Assume a n-type doped Si. There are 5 electrons in the M-shell of the dopant. One electron, the conduction electron, has a binding

energy of 10 to 50 meV. The Fermi level is very near the conduction band. For a p-type doped Si, the configuration is different. There are 3 electrons in the M-shell. One electron is missing, i.e. a hole. The Fermi level is very near to the valence band. Let us examine a p-n junction. From the considerations above, we can see that the net current of electrons and holes across the junction must be zero and that $pn = n^2$ at all points. From the cancellation of the current

$$-n(x)e\mu_e \frac{dV(x)}{dx} + eD_e \frac{dn(x)}{dx} = 0 \qquad \text{or} \qquad \mu_e \frac{dV(x)}{dx} = D_e \frac{1}{n}\frac{dn(x)}{dx}$$

where $V(x)$ is the potential, $n(x)$ is the electron density at a distance x from the junction, μ_e is the electron mobility and D_e is the electron coefficient of diffusion, $D = D_0 \exp(-\Delta W/\kappa T)$ and ΔW is the energy barrier. By integrating the current equation from well inside the n-side to well inside the p-side, we get

$$V_b = V_n - V_p = \frac{D_e}{\mu_e} \ln \frac{n_n}{n_p}$$

This potential difference is called the barrier potential. The barrier potential is generally lower than the band gap. In a state of equilibrium, the Fermi level is constant throughout the system as shown in Fig. 23. From an inspection of the voltage across the junction and integrating over the full length, X, of the depletion length, we see that

$$X = \sqrt{\frac{2\varepsilon V}{eN_d}} \qquad \text{and the capacitance} \qquad C(V) = \varepsilon \frac{A}{X}$$

where N_d is the number of donors and A is the area of the junction. If an external voltage is applied across the junction, the system is no longer in equilibrium and the Fermi level is no longer constant throughout the system. With a forward bias, V is reduced and thereby X is reduced as the bias voltage is subtracted from the barrier potential. A reverse bias adds to the barrier potential and the result is therefore a wider depletion layer.

The mobility and conductivity in a semiconductor is shown in Fig. 24. The volume resistivity for Ge is ≤ 0.49 Ωm at 300K whereas it is of the order of 100 Ωm in Si due to impurities. This will correspond for a Si crystal of $100 \times 100 \times 0.3$ mm^3 to $\sim 4 - 5\ 10^8$ free carriers. A minimum ionising particle would, in comparison, create $\sim 3 - 4\ 10^4$ e-h pairs. To reduce the number of free carriers, one can either deplete the crystal or do a freeze-out as shown in Fig. 24. Depletion by applying a forward bias is the most commonly used technique for particle detection. A possible lay-out is shown in Fig. 25. Depending of the detector configuration and the electronics that are used, space resolution of some 10 μm can be achieved. An introduction to semiconductors can be found in references [16] and [17].

3.3 Scintillators

A charged particle traversing matter leaves behind it a wake of ionisation, excited molecules and molecules in metastable states. Certain types of molecules will release a small fraction ($\sim$ 3%) of the absorbed energy as optical photons. Scintillating materials fall into one of two classes, organic or inorganic. An excited molecule can lose energy by vibration, dissociation or a resonance transfer to another molecule. It can also lose by emitting a photon. This is the scintillation or fluorescence. Fluorescence is prompt emission of photons as a result of an absorption of energy. The decay time of this photon emission is in the range from ns to μs. Let us first consider a perfect crystal structure as shown in Fig. 22c. The lifetime of a free hole is in the range of 10^{-12} s. This recombination may lead to photon emission, but it is too fast to be observed. The free electron might be trapped to the hole. This system is called an exciton. It is free to move through the crystal. The exciton can emit light when hitting

an activator center and transferring their binding energy to the activator levels, which will subsequently de-excite. Impurities or activators like Thallium, are therefore generally added to the crystal. In an imperfect crystal, there are lattice defects and impurities as shown in Fig. 26a. The excitation energy can here be dissipated not only by luminescence, but also by thermal dissipation, quenching, and by metastable levels, traps. The metastable systems will lose the energy either via thermal or vibrational dissipation or via a radiationless transition. The photon emission by luminescence can be written like

$$\frac{dL}{dx} = \frac{A}{1 + B\frac{dE}{dx}}\frac{dE}{dx} \qquad \text{or for small } dE/dx \qquad \frac{dL}{dx} \propto \frac{dE}{dx}$$

Table 3 gives selected physical properties of some inorganic crystalline scintillators. Note the fairly strong dependence on the light output as function of the temperature. Also the decay time is effected by the temperature. The light intensity as function of the wavelength is plotted in Fig. 26b.

The behaviour of organic scintillators are about the same as for inorganic. They are mainly based on benzene, C_6H_6. The p-electrons[1] forms the basis for the scintillation mechanism. They are quantised in series of singlets, S_{ij}, and triplets, T_{ij}, as in Fig. 27. A practical organic scintillator uses a solvent for the primary scintillation and then large concentration of a primary Fluor and smaller amount of secondary Fluor to shift down the final photon spectrum as indicated in Fig. 28a. The difference in wavelength between absorbed and emitted quanta, the Stokes shift, is shown in Fig. 28b. This shifting of the primary photon spectrum from a decay time of $\leq 10^{-9}$ s and a peak wave length of ~ 300 nm, is essential for an efficient photon detection as is discussed in section 3.4. Theory and application are well covered in reference [19].

3.4 Photon Detection

Photon detection around the visible spectrum is generally built around two processes, the photon to electron conversion, i.e. the photocathode, and the electron multiplication to generate a readable output signal. The operation of a photocathode is based on the photoelectric effect. For a semiconductor this may be considered as a three step process. In the first step, the photoelectron is excited from the valence band to the vacuum level by the absorption of the light quanta. The second step is to transport the excited electron through the semiconductor film to the semiconductor/vacuum interface. The third step is an escape over the surface barrier into the vacuum. The efficiency of the photoelectric emission is determined by the efficiency in each step. At the surface of a semiconductor there is always some bending of the energy bands due to the presence of donors and acceptors with energy levels in the forbidden zone. See 3.2 for discussion of the energy bands. p-type materials are therefore the most efficient photoemitters. These are semiconductors like $(Na_2KSb)Cs$, Cs_3Sb and GaAs:Cs·O. The emission energy for the photoelectron excited by a monochromatic light, will range from zero to a maximum given by $E_{\text{light}} - [E_{\text{electron affinity}} + E_{\text{gap width}}]$. In addition to photoemission, the photocathodes will also produce thermionic emission. This will present itself as an unwanted background. A summary of photocathode characteristics is given in Table 4. These photocathodes are very sensitive to air and will easily oxidise. They must therefore be deposited and operated in ultra high vacuum. There is another type of photocathodes that can be operated in an inert gas. They

[1]Some bonds in benzene [18]: Benzene is a planar molecule with six C-C bond distances of equal length. The observed bond distance (1.40 angstroms) is midway between the sp^2-sp^2 single-bond distance (1.46 angstroms) and sp^2-sp^2 double-bond distance (1.34 angstroms) seen in conjugated dienes and is consistent with the bond order of 1.5 predicted by resonance theory. (Bond order is an index of bond strength. A bond order of 1 indicates that a single s bond exists between two atoms, and a bond order of 2 indicates the presence of one s and one p bond between two atoms. Fractional bond orders are possible for resonance structures, as in the case of benzene.) Benzene is a regular hexagon; all bond angles are 120°.

are mainly used as an additive to the gaseous detectors. Some properties of these components are listed in Table 5. CsI, an alkali halide crystal, which falls into the first category, is used successfully as a solid photon converter in gaseous detectors. Quantum efficiency for some photocathodes are plotted in Fig. 29.

The electron amplification process in a gaseous detector is described in 3.1. In a vacuum tube, the secondary-electron process is used. The process of secondary-electron emission is similar to photoemission. It is different for metals than for insulators or semiconductors. When a clean metal surface is exposed to an energetic primary electron, the secondary-electron emission takes place by raising the energy level in the conduction band to the one of the vacuum level. One primary electron may have sufficient energy to excite one or more secondary electrons. Clean metals are poor secondary-electron emitters whereas insulators and semiconductors are efficient. Clearly the electron affinity plays a crucial role and an efficient secondary-electron emitter should have an E_A zero or negative.

From the discussion above, a photon detector is therefore either a gaseous detector where a photosensitive vapour has been added to the gas or a vacuum tube with a photocathode and electron multiplication based on secondary-electron emission. The microchannel plate is an example of the latter. A microchannel plate is a two dimensional array of microchannels as shown in Fig. 30a. The microchannel itself has an internal diameter of 8 to 45 μm and is lined by a resistive secondary emission film. The schematics of a photoelectron multiplier tube is shown in Fig. 30b. Dynodes of secondary-electron emitters are placed in the voltage chain between the photocathode and the anode. The total current gain is equal to the product of the current gain at each dynode. The production of secondary electrons is Poissonian distributed. The fluctuations on the final number is therefore mainly induced at the first dynodes where the number of primary electrons are small.

The novel hybrid photo diodes [22] is a vacuum tube with a semitransparent photocathode, a focusing accelerating field and a silicon sensor at the anode, see Fig. 30c. The primary photoelectron will have a kinetic energy of 10 to 20 keV when it impinges onto the sensor and will produce in the order of 4 to 5000 electron-hole pairs. This ensures a very good signal resolution. For further reading on photon detectors, references [20] and [21] are recommended.

4 Detection Systems

Charged particle detection is already covered in sections 3.1, 3.2 and 3.3. We will in this section look into some composite systems and also include detection of uncharged particles.

4.1 Particle Identification

The condition for Cherenkov radiation was given on page 4. The Cherenkov photons of wavelength λ are emitted under an angle Θ_C, where Θ_C is given by $\cos\Theta_C = 1/[\beta n(\lambda)]$ and the number of photons emitted by

$$\frac{dN}{d\lambda} = 2\pi\alpha \left(\frac{q}{\lambda}\right)^2 L \sin^2\Theta_C$$

L is the length, $n(\lambda)$ is the refractive index of the radiator and $\alpha = 1/137$ is the fine-structure constant. The total number of photons emitted between λ_1 and λ_2 by a singly charged particle is then given like

$$N[\lambda_1 \to \lambda_2] = 4.6\ 10^6 \left[\frac{1}{\lambda_2(\text{Å})} - \frac{1}{\lambda_1(\text{Å})}\right] L(\text{cm}) \sin^2\Theta_C$$

The number of detected photons is equal to the total number of emitted photons multiplied by the quantum efficiency of the detection system. If the momentum p of the particle is determined as discussed on page 5, the mass, m, of the particle is given by $m = p/\beta\gamma$. The uncertainty of the mass measurement is given by

$$\frac{\Delta m}{m} = \sqrt{\left(\frac{\Delta p}{p}\right)^2 + (\gamma^2 \tan\Theta_C \ \Delta\Theta_C)^2}$$

We can therefore use the measurement of the Cherenkov angle and the knowledge on the momentum of the particle to make mass hypothesis for the charged particle.

Cherenkov detectors consist of a radiator with a refractive index n and a photon detector. They are frequently categorised into two classes, the threshold detector and the ring imaging detector. The threshold detector will discriminate between particles where $\beta n > 1$ and particles below this threshold. They are mainly used in monochromatic beams to discriminate between particles of different masses. The ring imaging detector [23] exploits simultaneously more or less all the properties of Cherenkov radiation. That is, the existence of a threshold, the dependence of the number of photons, the dependence on the charge of the particle and the dependence of the Cherenkov angle. A practical detector will need to have a high efficiency for single photon detection and have a high space resolution. Cherenkov detectors are sketched in Fig. 31.

In the same way as we have done for the Cherenkov radiation, we can construct a detection system for transition radiation. Transition radiation is discussed on page 4. We recall that the total radiated power in eV is about 1 % of γ of the particle and that the angle of maximum radiation is very forward peaked as it is inversely proportional to γ. The energy of the emitted radiation has to be much larger than the plasma frequency of the radiator material and will in general be between 1 and 10 keV. A practical transition radiation detector will therefore consist of a radiator with many interfaces or foils and a detector for soft x-rays. The foils will be of low Z-material in order to limit the scattering and the detector could be proportional chamber based on Xenon for a maximum conversion efficiency. The number of foils is a trade-off between production of x-rays and the absorption of them. The detection of electrons from the converted x-ray is also made difficult by the fact that they are very near to the trajectory of the particle and therefore the ionisation caused by the particle in the gas of the detector. A high energy particle will create ~ 200 electron-ion pairs per cm in Xe gas at NTP. The conversion of a 5 keV x-ray will create ~ 400 electron-ion pairs. The detector is therefore usually thin in order to enhance the discrimination power of the detector. One finds in general [25] that

$$\frac{\text{ionisation + detected transition radiation}}{\text{ionisation}} \sim Z^{-\frac{7}{2}}$$

Transition radiation detectors are used for e to π separation.

Particle identification by measuring the energy loss by the charged particle in matter, is discussed in section 3.1. We will here only recall that this technique generally calls for a rather thick gas volume where many samples of the energy loss are taken along the track. As for the other identification methods, it is assumed that the momentum of the particle is determined by other means.

Particle identification can also be done by measuring the time difference between detection points along the particle track. This is the Time-of-Flight, TOF, technique. It is similar to the Cherenkov detection as it is a pure measurement of the β of the particle. A TOF measurement can in principle be used for any value of β. A TOF system will typically be a large hodoscope of scintillators coupled to a photomultiplier read-out system for a measurement of the impact time, T_1, at this distance from the vertex, together with a knowledge of the time T_0. T_0 is

the creation time of the event or the bunch crossing of the particle beams in the experiment. It could also be a smaller hodoscope placed very near to the vertex of the event. For certain applications, it is also possible to forego the T_0 by assuming that one of the particles detected in the far hodoscope has a velocity $\beta \simeq 1$. With the measurement of the time difference and the track length, β of the particle is known. A small uncertainty on the time measurement is required in order to keep the track length inside reasonable limits and thereby limit the size of the hodoscope. Other fast detectors can be used. Some of them are discussed in [26] and [27]. A summary on particle identification is given in Table 6.

4.2 Calorimeters

A class of detectors measures the energy and the position of particles through total absorption in these detectors. In the process of absorption, secondary particles are generated. These secondary particles will as well react inside the detector. The process gives rise to a shower. The growth and decay of a shower is a tremendously complex statistical process where several physical mechanisms participate. The net result is however that the initiating particle is expanded in ionisation and ultimately in heat. The temperature gradient and the shock wave accompanying can be measurable. We will discuss the atomic excitation and ionisation which is created in the shower process and leave the calorimetric[2] effect here. There are several reasons why the calorimeters are attractive. They are the only way to detect and measure neutral particles and as the absorption of the energy of the particle is a statistic process, the precision of the energy measurement of the particle should therefore be proportional to $1/\sqrt{E}$. From the discussion of the momentum measurement on page 5, we see that $\sigma_p/p^2 \propto \sigma_{R\phi}/\left(L^2 B\right)$ in a spherical coordinate system. A calorimetric measurement can therefore become more accurate than a measurement of the curvature of the particle track in a magnetic field.

Calorimeters are normally classified into two main groups. The electromagnetic and the hadronic calorimeters. They are, as the name indicate, optimised for measuring particles that interact electromagnetically or has strong interactions with the absorbing material. Subclass of each are the sampling calorimeters and the homogeneous calorimeters. Fig. 32a shows the development of electromagnetic showers. Fig. 32b and c shows sketches of these detectors.

Electron pair production and Bremsstrahlung are the dominant interaction process for high energy photons and electrons. From Fig. 7a, we see that Bremsstrahlung is nearly independent of energy above ~ 1 GeV. The same is the case for pair production which is plotted in Fig. 8. The secondary particles in the electromagnetic shower are electrons, positrons and photons and they will interact with the matter in the same way as the parent particle. The number of particles in the shower will therefore increase until the average energy of the particles is below a threshold to stop further particle creation. The shower will then spend its energy in ionisation or Compton scattering and will slowly die off. The change of the relative strength of the interaction processes are characterised by the critical energy, E_C, of the material. (See the discussion on page 3 and Fig. 7b.) The lateral development of the shower is mainly governed by the electrons that do not radiate, but have enough energy to travel far away from the axis. From this rather sketchy discussion of the electromagnetic shower which follows the Rossi II approximation on page 3, we see that the natural unit to express the shower in, is in units of radiation length, X_0. The shower maximum will be different for electrons and for photons. Experiments have shown that

[2] From [18]: Calorimeters have been designed in great variety. One type in widespread use, called a bomb calorimeter, basically consists of an enclosure in which the reaction takes place, surrounded by a liquid, such as water, that absorbs the heat of the reaction and thus increases in temperature. Bomb calorimeters have been developed to the point that heats of combustion of organic materials can be measured with results reproducible within 0.01 percent.

for an initiating particle of energy E, the shower maximum in units of X_0 is

$$t(X_0) = \ln \frac{E}{E_C} - 1.0 \quad \text{for electrons} \qquad t(X_0) = \ln \frac{E}{E_C} - 0.3 \quad \text{for photons}$$

The lateral shower spread is expresses in Molière units. It is defined as

$$R_M = \frac{(\text{Characteristic Energy})(\text{Radiation Length})}{\text{Critical Energy}} = 21\,[\text{ MeV}]\,\frac{X_0}{E_C} \propto \frac{A}{Z}\left[\frac{\text{g}}{\text{cm}^2}\right]$$

~ 95 % of the shower is contained inside a cone with radius $2R_M$. The longitudinal track length, which is proportional to the energy deposit, is well approximated to

$$T = \mathcal{F}(z)\frac{E}{E_C}X_0 \quad \text{where } \mathcal{F}(z) \simeq e^z\left[1 + z\ln\frac{z}{1.526}\right] \quad \text{and} \quad z = 4.58\frac{Z}{A}\frac{E_{\text{cut-off}}}{E_C}$$

The cut-off energy, $E_{\text{cut-off}}$, is the minimum energy of a particle that can be detected in the calorimeter.

For a sampling electromagnetic calorimeter as sketched in Fig. 32b, let us assume that we sample N times the energy deposited by the shower. Let x be the distance along the shower axis between each sample. Let us furthermore assume that each sample is statistically independent. For large N, the energy resolution can then be written like

$$\frac{\sigma(E)}{E} = 3.2\%\sqrt{\frac{E_C}{\mathcal{F}}}\sqrt{\frac{x}{X_0}}\sqrt{\frac{1}{E}}$$

The development of a hadronic shower is much more complex than the electromagnetic processes. It is mainly propagated by hadronic interactions. At high energies, these processes are characterised by multi particle production and particle emissions from nuclear disintegration of excited nuclei. Due to the relatively frequent generation of π^0-s, there is also an electromagnetic component present in hadronic showers. A sizeable amount of the available energy is converted into excitation and break-up of nuclei. Only a small fraction of this energy will eventually appear as detectable signal and with large event-to-event fluctuations. The hadronic multiplication process is measured by the nuclear interaction length, λ_I, which is nearly energy independent. λ_I is practically proportional to $A^{1/3}$ as shown in Fig. 9. Some characteristics for high energy hadronic showers may be written like
Shower maximum

$$l_{max} \approx [0.6\log(E) - 0.2]\,\lambda_I \quad \text{, with } E \text{ in GeV}$$

Shower depth for 95 % longitudinal containment:

$$l_{95\%} \approx l_{max} + 4E^{0.15}\lambda_I \quad \text{, with } E \text{ in GeV}$$

Contrary to electromagnetic showers, which develop in sub-nanosecond time, the physics of hadronic showers is characterised by different time scales, the slowest of which, de-excitation of heavy nuclei, may reach a microsecond. Massive hadron calorimeters are commonly used for the detection of neutrinos, as the secondaries from weak interactions are mostly hadrons.

In a sampling calorimeter, Fig. 32b, the particle absorption and shower sampling is separated. A fraction of the total energy is sampled in the active detector. The active detector can be any of the detectors that we have discussed above, like scintillators, ionisation chambers, wire chambers or solid state detectors. The particle absorbers in an electromagnetic calorimeters will be of low X_0 material like lead. A hadronic calorimeter will use material like iron, with long λ_I. The energy resolution for a large sampling electromagnetic calorimeter will be in the range of 10 % at 1 GeV. For large volume sampling hadronic calorimeters, it will be in the order of 80 %.

The reason for this moderate energy resolution in a hadron calorimeter, is the large fluctuations as a fair fraction of the incident energy is spent in back-scattering, energy leakage by muons, neutrinos and slow neutrons. In addition, a large fraction is lost by nuclear excitation and nucleonic evaporation. All these processes do not give an observable signal in the detector. This can be demonstrated by measuring the ratio of a signal from an electron and a signal from a hadron. This is the electron-hadron ratio, e/h. If $e/h = 1.0$, the calorimeter is said to be compensating. If it differs from unity by more than 5 % or 10 %, detector performance is compromised because of fluctuations in the π^0 content of the cascades. In most cases e/h is greater than unity, particularly if little hydrogen is present. Energy resolution of $30 - 40\ \%/\sqrt{E}$ has been demonstrated for a well compensated hadronic sampling calorimeter [25] [29] [30].

In a fully active and homogeneous electromagnetic calorimeter as shown in Fig. 32c, the energy is typically measured by collecting photons as these detectors are normally made from low X_0 scintillators as in Table 3. In other material like lead glass, 55 % PbO and 45 % SiO_2, the light emission is by Cherenkov radiation. The energy resolution is limited by photon statistics. If we take a scintillating crystal, which is virtually free from intrinsic fluctuations, we get

$$\frac{\sigma(E)}{E} = \frac{1}{\sqrt{N_{pe}}} = \frac{1}{\sqrt{E(\mathrm{GeV})}\sqrt{N_{pe}/\mathrm{GeV}}}$$

where N_{pe}/GeV is the observed number of photons per energy unit. To get this number, the absolute light yield, the number of emitted photons for each energy unit, has to be multiplied with the light collection efficiency, the geometrical efficiency of the photon detector and the quantum efficiency integrated over the emission spectrum. In addition, there will be effects from lateral shower leakage, the punch-through and the material in front of the detector. $\sigma(E)/E$ in lead glass will be in the range of $\geq 5\%E^{-\frac{1}{2}}$ whereas for NaI(Tl) it will be in the range of $\geq 1.5\%E^{-\frac{1}{4}}$ for E in GeV.

For real calorimeters in real experiments, the energy resolution is usually written as

$$\frac{\sigma(E)}{E} = \frac{a}{\sqrt{E}} \oplus b \oplus \frac{c}{E}$$

where a is the stochastic term. b is a constant term which normally describes the overall inter-calibration. c is the contribution from the electronics noise. Energy resolution for some homogeneous electromagnetic calorimeters in large experiments is given in Fig. 33. We see that the energy resolution for the BGO calorimeter in this experiment is well described by the parameters: $a \simeq 1.9\ 10^{-2}$, $b \simeq 5\ 10^{-3}$ and $c \leq 10^{-4}$. About 5400 crystals constituted the calorimeter. The final overall resolution compares well to the test beam result, which was given as $\sigma(E)/E = \left[1.54/\sqrt{E} + 0.38\right]$ %.

The complex computation of shower development is well described in simulation programs like [31]. References [29, 30] discuss the physics of electromagnetic and hadronic calorimeters.

5 Conclusion

We have in this write-up looked into the more general considerations of particle detection and left out many aspects that make a detector a success or a failure. Electronics [33], Trigger/DAQ and Data Analysis are taken care of in separate lectures. We have, though, left out all the magic, the witchcraft and we will not even mentioned the Hopi Snake dance which has proven most useful in cases of high voltage break-down. The Ouija board becomes handy when the answer can not be found on the Web and no trace of the book listed in the references can be found in the library. At no point was all the hard work which is the essential component to a working detector discussed. Obnoxious things like detector ageing has been happily swept under the carpet together with the most valuable detector control systems. It can nonetheless be a useful precaution to check the detector performance against Ohm's law if the fuses keeps popping and against Newton's laws of motion if the detector keeps falling down.

Disclaimer

The numbers, formulae, figures and references are believed to be correct, but are not guaranteed to be so.

and Acknowledgement

At the end, I will thank all my collaborators and in particular Erich Albrecht, Tito Bellunato, Ariella Cattai, Carmelo D'Ambrosio, Martyn Davenport, Marcella Diemoz, Thierry Gys, Christian Joram, Wolfgang Klempt, Stefan Koestner, Martin Laub, Georg Lenzen, Dietrich Liko, Niko Neufeld, Gianluca Aglieri Rinella, Dietrich Schinzel and Ken Wyllie for their help to make both the lectures and the write-up.
I also hope you have had as much sweat, tears and fun reading this as I have had in writing it.

References

[1] Dan Green, The Physics of Particle Detectors, Cambridge University Press; ISBN: 0521662265
Claus Grupen et al., Particle Detectors, Cambridge University Press; ISBN: 0521552168
K. Kleinknecht, Detectors for Particle Radiation, Cambridge University Press; ISBN: 0521648548
Glenn F. Knoll, Radiation Detection and Measurement, John Wiley & Sons, ISBN: 0471073385
try also
http://icfa3d.web.cern.ch/ICFA3D/3D/html2/node1.html

[2] John David Jackson, Classical Electrodynamics, John Wiley & Sons; ISBN: 047130932X
Additional reading
David J. Griffiths, Introduction to Electrodynamics, Prentice Hall PTR; ISBN: 013805326X
Richard Phillips Feynman, The Feynman lectures in physics, Addison-Wesley; ISBN: 0201510030

[3] D.E. Groom et al., The Review of Particle Physics, The European Physical Journal C15 (2000) 1, http://pdg.web.cern.ch/pdg/

[4] J. Va'vra, Particle identification methods in high-energy physics, Nuclear instr. and methods A 453(2000)262-278

[5] B. Rossi, High Energy Particles, Prentice-Hall Inc., Englewood Cliffs, NJ, 1952.

[6] W.W.M. Allison and P.R.S. Wright, RD/606-2000-January 1984

[7] V. Egorytchev and V.V. Saveliev, Monte Carlo simulation of transition radiation and electron identification for HERA-B, ITEP-99-11

[8] B. Dolgoshein, Transition radiation detectors, Nucl. Instrum. Methods Phys. Res., A 326(1993)434-469

[9] Opera-3D version 7.005, Vector Fields Limited, 24 Bankside, Kidlington, Oxford OX5 1JE, England
John S. Beeteson, Visualising Magnetic Fields, Academic Press, Incorporated, ISBN: 0120847310

[10] L.C.L. Yuan and C. Wu, Nuclear Physics, in Methods of Experimental Physics, L. Marton ed., Academic Press, New York (1961), Vol. 5, Part A

[11] F. Sauli, Principle of Operation of Multiwire Proportional and Drift Chambers, CERN 77-09, 3 May 1977.

[12] Leonard B. Loeb, Basic Processes of Gaseous Electronics, University of California Press, 1955.

[13] Rob Veenhof, Garfield Version 7.02, http://ref.cern.ch/CERN/CNL/2000/001/Pr/garfield

[14] G. Charpak (*ed*), Research on Particle Imaging Detectors, World Scientific, ISBN: 9810219024

[15] L. Landau, J. Physics (USSR) 8 (1944) 201
or see
http://rkb.home.cern.ch/rkb/PH14pp/node1.html

[16] D. A. Fraser, The physics of semiconductor devices, Clarendon Press, ISBN: 0198518595

[17] J. Wilson and J. F. B. Hawkes, Optoelectronics An Introduction, Prentice/Hall, ISBN: 0136383955

[18] Encyclopedia Britannica Reference Suite, Encyclopedia Britannica, Incorporated, ISBN: 0852296746

[19] J.B. Birks, The Theory and Practice of Scintillation Counting, Pergamon, London, 1964.
Pieter Dorenbos (*ed*) and Carel W. Van Eijk (*ed*), Inorganic Scintillators and Their Applications: Proceedings of the International Conference, Scint 95, Coronet Books, ISBN: 9040712158
Harley Ross (*ed*), John E. Noakes (*ed*) and Jim D. Spaulding (*ed*), Liquid Scintillation Counting and Organic Scintillators, Lewis Publishers, ISBN: 0873712463

[20] I. P. Csorba, Image Tubes, Howard W. Sams & Co., ISBN: 0672220237

[21] J. Séguinot, Les Compteurs Cherenkov, CERN-EP/89-92, LPC/89-25

[22] C. D'Ambrosio et al., The ISPA-tube and the HPMT, two examples of a new class of photodetectors: the hybrid photo detectors, 5th International Conference on Advanced Technology and Particle Physics : ICATPP-5, Como, Italy, 7 - 11 Oct 1996, J - Nucl. Phys. B, Proc. Suppl. : 61B (1998)
M. Alemi et al., Performance of a hybrid photon detector prototype with electrostatic cross-focussing and integrated silicon pixel readout for Cherenkov ring detection, Nucl. Phys. B, Proc. Suppl.: 78 (1999)
C. Joram, Large area hybrid photodiodes, Nucl. Phys. B, Proc. Suppl. : 78 (1999)

[23] T. Ypsilantis and J. Séguinot, Theory of ring imaging Cherenkov counters, Nucl. Instrum. Methods Phys. Res., A: 343 (1994)
J. Séguinot and T. Ypsilantis, A historical survey of ring imaging Cherenkov counters, Nucl. Instrum. Methods Phys. Res., A: 343 (1994)

[24] R. Forty and O. Schneider, RICH pattern recognition, LHCb-99-010, 27 May 1999

[25] C. W. Fabjan and H. G. Fischer, Particle Detectors, Reports on Progress in Physics, 143 (1980), CERN-EP/80-27, 6 March 1980

[26] H. R. Schmidt, Pestov spark counters: work principle and applications, Nucl. Phys. B, Proc. Suppl.: 78 (1999)
A. V. Akindinov et al., The multigap resistive plate chamber as a time-of-flight detector, Nucl. Instrum. Methods Phys. Res., A: 456 (2000)

[27] W. Klempt, Review of particle identification by time of flight techniques, Nucl. Instrum. Methods Phys. Res., A: 433 (1999)

[28] Robert B. Leighton, Principle of Modern Physics, McGraw-Hill Book Company, 1959

[29] R. Wigmans, Calorimetry in high-energy physics, Academic Training Lectures, CERN, Geneva, Switzerland, 1988-1989.
R. Wigmans, Calorimetry: Energy Measurement in Particle Physics, Oxford Science Publications, 2000, ISBN 0 19 850296 6

[30] U. Amaldi, Fluctuations in Calorimetry Measurements, Physica Scripta, 23(1981)
C.W. Fabjan, Calorimetry in High-energy Physics, in: Experimental Techniques in Nuclear and Particle Physics, T.Ferbel (*ed*), World Scientific, 1991

[31] J.P. Wellisch, Physics of shower simulation at LHC, at the example of GEANT4, Academic Training Lecture Regular Programme 01 - 04 March 2004
http://geant4.web.cern.ch/geant4/
M. Asai, Introduction to Geant4, 23rd CERN School of Computing, Marathon, Greece, 17 - 30 Sep 2000 / Ed. by Vandoni, C E - CERN, Geneva, Dec 2000. [CERN-2000-013]
The online version of the FLUKA manual (*fluka99.manual*)
http://fluka.web.cern.ch/fluka/material/Fluka/head.html

[32] E. Longo, Calorimetry with crystals, 8th International Conference on Calorimetry in High Energy Physics, Lisbon, Portugal, 13 - 19 Jun 1999 - World Sci., Singapore, 2000.

[33] V. Radeka, Signal processing for radiation detectors, Academic Training Lectures, CERN, Geneva, Switzerland, 1 Sep 1985 - 30 Jun 1986
Zoher Z. Z. Karu, Signals and Systems Made Ridiculously Simple, ZiZi Press, ISBN: 0964375214
Joseph J. Carr, Natalie F. Harris (Editor), Electronic Circuit Guidebook Vol 3: OP AMPS, Sams, Howard W. and Company, ISBN: 0790611317
A.J. Peyton, V. Walsh and Y. Walsh, Analog Electronics with Op Amps: A Source Book of Practical Circuits, Cambridge University Press, ISBN: 052133604X
Antonio L. Zichichi, Gas Detectors and Electronics for High Energy Physics, World Scientific Publishing Company, ISBN: 9810211481

Gas	A $cm^{-1}Torr$	B $Vcm^{-1}Torr$
He	3	34
Ne	4	100
Ar	14	180
Xe	26	350
CO_2	20	466

Table 1: Parameters for the Korff approximation for the first Townsend coefficient α [11].

Type of dopant	Donor	Acceptor
Semiconductor type	n-type	p-type
Majority carrier	electrons	holes
They occur in the	conduction band	valence band
Minority carrier are	holes	electrons
Possible dopant in Si or Ge	P, As, Sb	B, Al, Ga
Dopant in group	5	3
Charge in ionised dopant is	+ve	-ve
Fermi level is nearer	conduction band	valence band

Table 2: A list of a number of pairs of terms that go with donors or acceptors [16].

Crystal	BGO	CsI:Tl	CsI	PWO	NaI:Tl
Density g/cm^3	7.13	4.53	4.53	8.26	3.67
Radiation length cm	1.12	1.85	1.85	0.89	2.59
Wave length nm	480	565	310	420	410
Light yield ($\mathcal{L}$) % of NaI	10	85	7	0.2	100
Decay time ns	300	1000	6+35	5+15+100	250
$d\mathcal{L}/dT$ %/°C at 18°C	-1.6	0.3	-0.6	-1.9	0
Refractive index	2.15	1.8	1.8	2.29	1.85

Table 3: Physical properties of some inorganic scintillators. BGO is bismuth germanate and PWO is lead tungstate.

Cathode	Peak λ (Å)	Maximum Quantum Yield at peak (%)	λ_0 (Å) [at 1 % of peak]	Maximum (μA/lm)	Typical Thermionic Emission (A/cm^2)	E_g (eV)	E_A (eV)
Ag-O-Cs	8000	0.5	$\simeq$ 12000	60	10^{-12}		
Cs_3Sb on MnO	4000	20	6500	80	10^{-15}	1.6	0.45
(Cs)Na_2KSb	4000	30	9500	550	10^{-15}	1.0	0.35
K_2CsSb	4000	30	6600	100	$< 10^{-17}$	1.0	0.90
Na_2KSb	4000	30	6600	130	$< 10^{-17}$	1.0	0.75
GaAs:Cs·O	7800	> 20	9500	> 1000	$< 10^{-14}$	1.4	< 0

Table 4: Summary of photocathode characteristics [20]. E_g is the energy gap between valence and conduction band. E_A is the electron affinity or the energy gap between the conduction band and the vacuum level.

Molecule		Ionisation energy (eV)	p_0 at 300K (Torr)
Ethanol	C_2H_5OH	10.4	47
Acetone	$CH_3(CO)CH_3$	9.69	250.7
Benzene	C_6H_6	9.24	101.8
TEA	$(C_2H_5)_3N$	7.5	73.2
TMAE	$C_2[(CH_3)_2N]_4$	5.36	0.50

Table 5: Physical properties of some possible gaseous photon converters [21]. TEA is Triethyl amine and TMAE is Tetrakis(dimethylamino)ethylen. See also Fig. 29b.

Technique	γ range	Comments	
Multiple ionisation measurements in homogeneous medium	$\gamma < 6$	As $dE/dx \stackrel{\sim}{\propto} 1/\beta^2$ for $\gamma \leq 6$, powerful discrimination obtainable with modest resolution in the dE/dx measurement.	[4]
Time-of-Flight	$\gamma \leq 6$	$\sigma \leq 300$ ns has been achieved with large scintillator systems. $\sigma \leq 100$ ns with special spark chambers	[27]
Gas threshold Cherenkov	$\gamma > 10$	Not suitable for storage ring application where 4π coverage is required.	[21]
Multiple ionisation measurements on relativistic rise in homogeneous medium	$2 \leq \gamma \leq 50$	Requires $\sigma(dE/dx) \sim 2-3$ %; achieved so far in planar geometry only, but not in storage ring application.	[4]
Imaging Cherenkovs	$2 < \gamma \leq 200$	Cherenkov photons detected with UV-sensitised proportional chamber structures; or special optical systems, with severely limited phase-space acceptance for particles.	[23]
Transition radiation	$\gamma \geq 1000$	Useful as compact threshold detector for specialised applications.	[8]

Table 6: Table from [25]. It was published in 1980, just 10 years after the first publication by G. Charpak on proportional chambers and 3 years after the first publication of J. Séguinot and T. Ypsilantis on ring imaging Cherenkov detectors. 1974 was the year of the first publication on drift chambers by G. Charpak and collaborators. References to updated numbers has been added as a last column to the table.

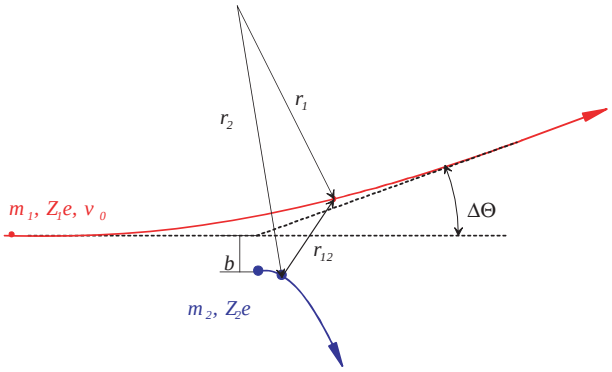

Figure 1: Rutherford scattering

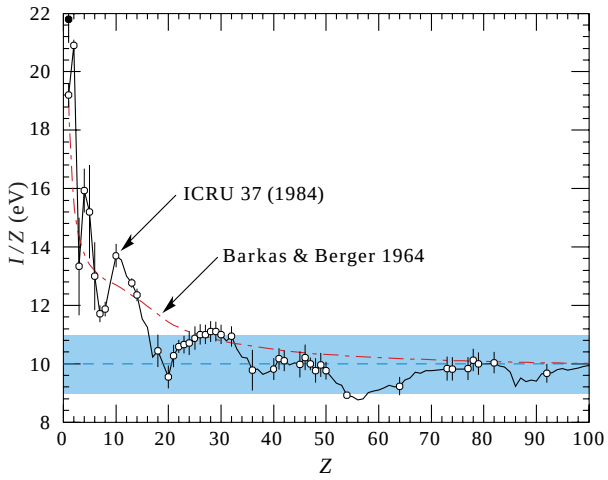

Figure 2: Excitation energy divided by Z [3]

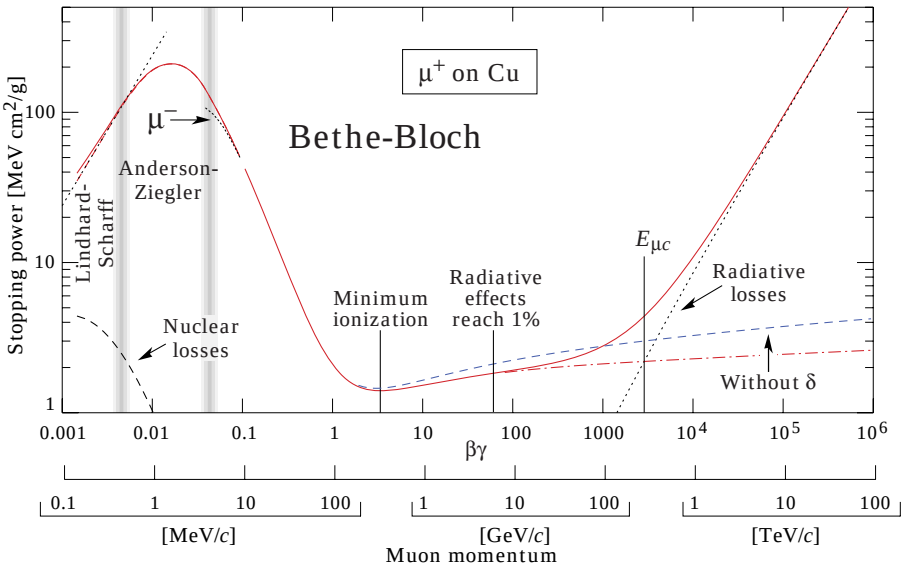

Figure 3: Energy loss rate in copper [3]

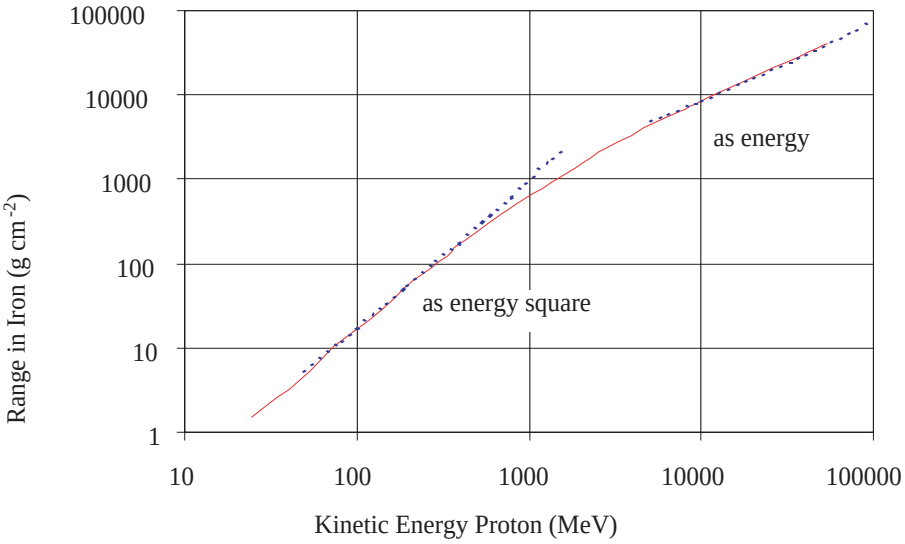

Figure 4: Range of proton in iron

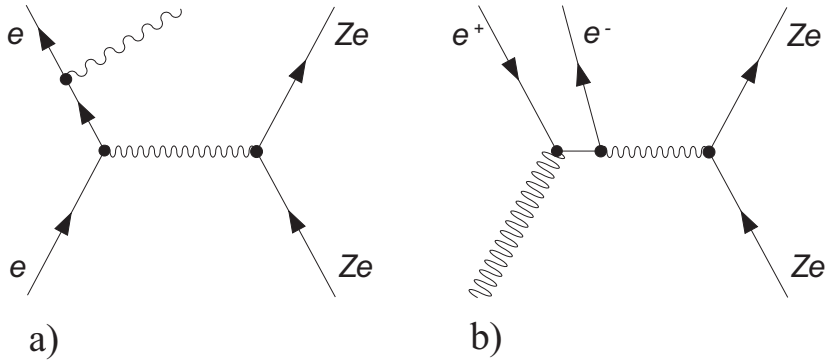

Figure 5: Feynman diagram for a) Bremsstrahlung and b) Pair production

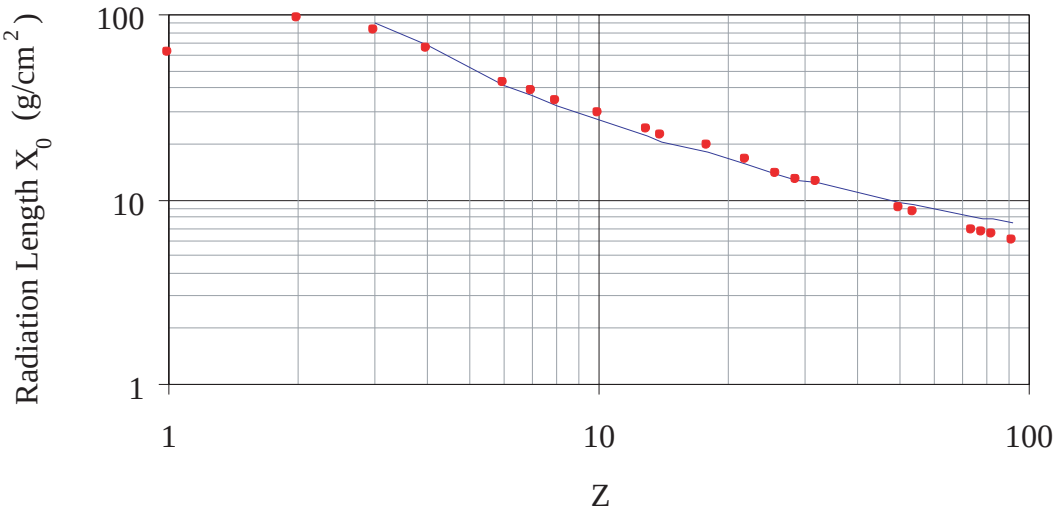

Figure 6: Radiation length as function of Z. The solid line is a fit to A/Z^2.

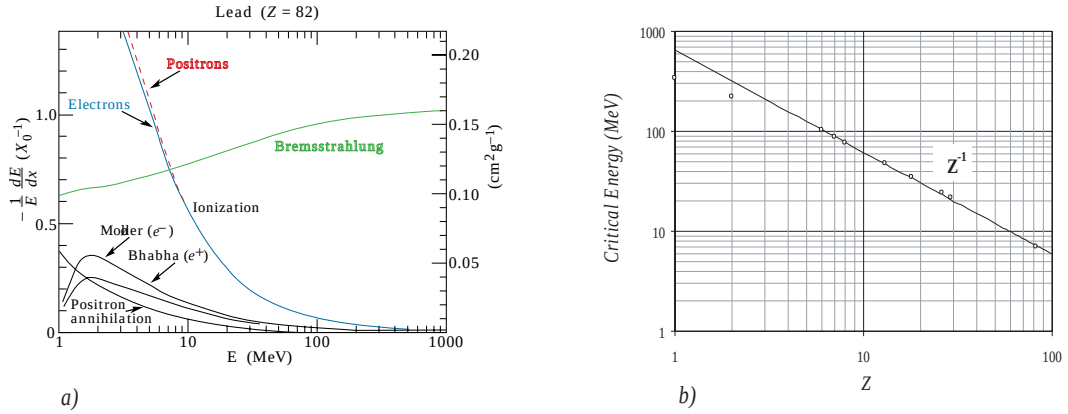

Figure 7: a) Fractional energy loss per radiation length in lead as function of positron or electron energy [3] b) Critical energy as function of Z

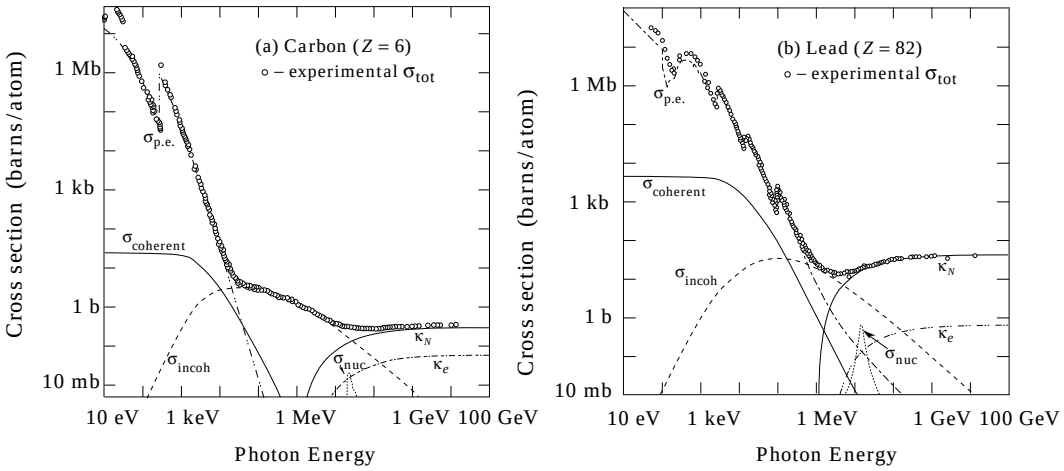

Figure 8: Photon total cross section as function of energy in carbon and lead [3]. Where $\sigma_{\text{p.e.}}$ is the Atomic photo-effect, σ_{coherent} is the Coherent scattering (Rayleigh scattering), $\sigma_{\text{incoherent}}$ is the Incoherent scattering (Compton scattering), κ_n is the Pair production in nuclear field, κ_e is the Pair production in electron field and σ_{nuc} is the Photonuclear absorption.

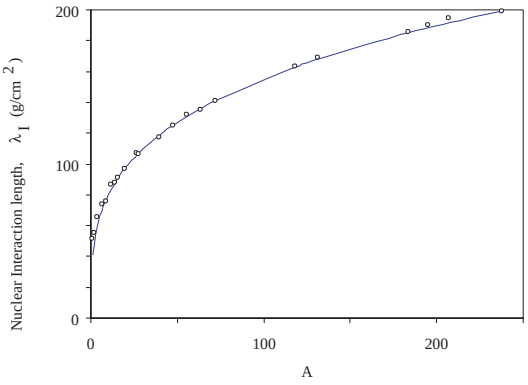

Figure 9: Nuclear interaction length, λ_I, as function of A. The line is a fit to $\lambda_I \propto A^{0.29}$.

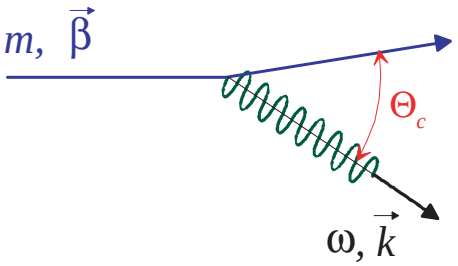

Figure 10: Charge particle interaction with matter.

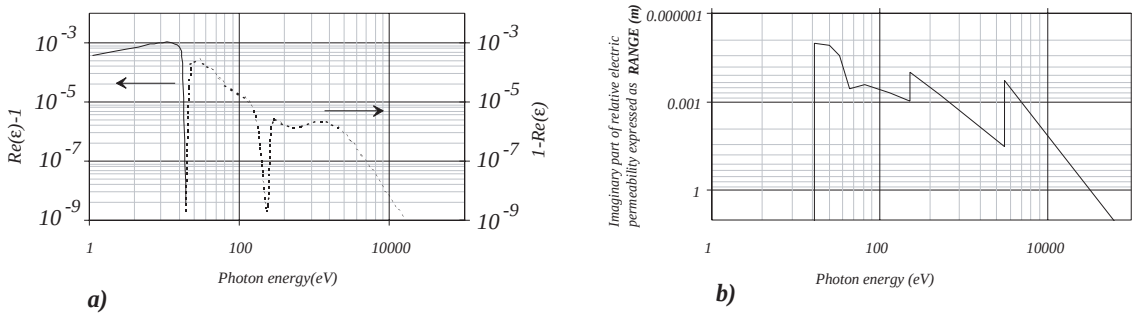

Figure 11: The real (a) and imaginary (b) part of the relative electric permeability of argon as function of the photon energy [6].

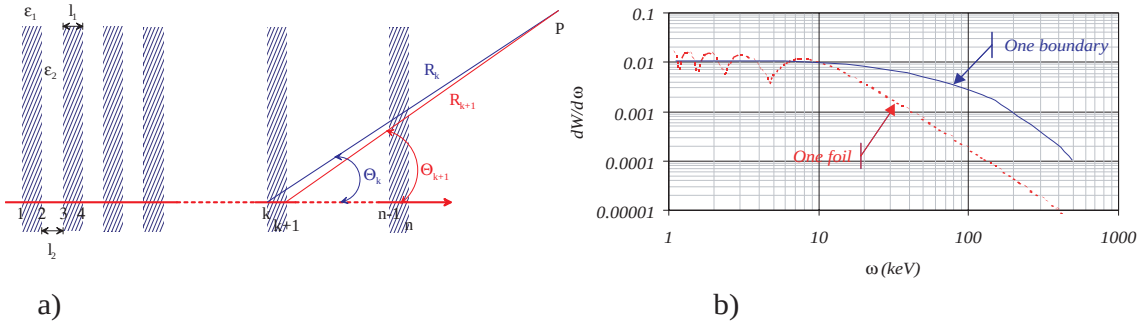

Figure 12: A periodic transition radiator, a, with coherent addition in point P. Figure b from [7] for $\gamma = 2 \cdot 10^4$, l_1=25 μm , l_2=0.2 mm and for polypropylene and air.

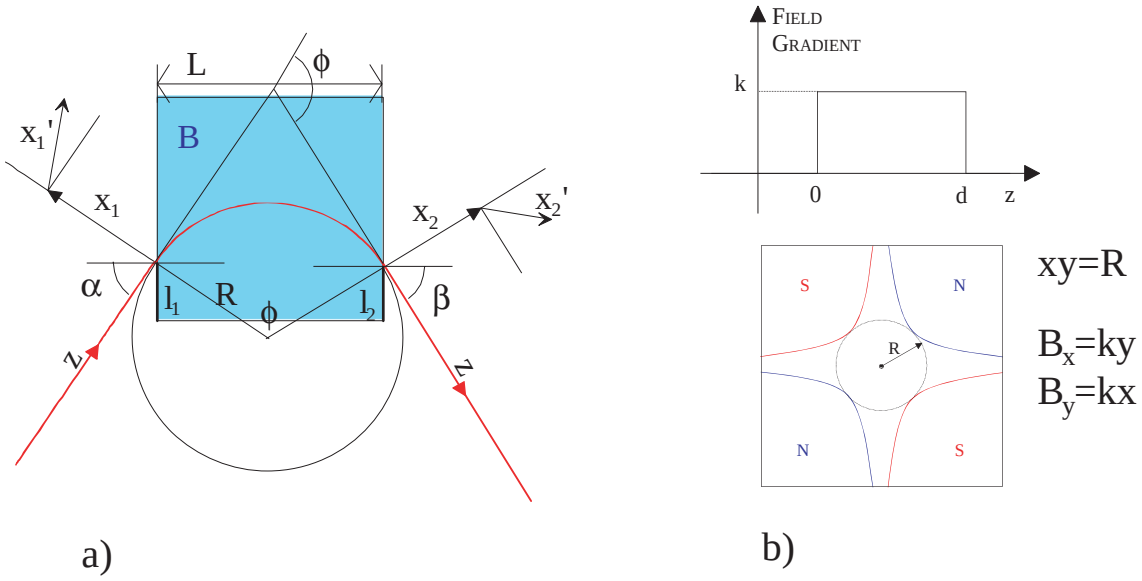

Figure 13: Figure a) is a rectangular bending magnet. b) is for an ideal quadrupole configuration.

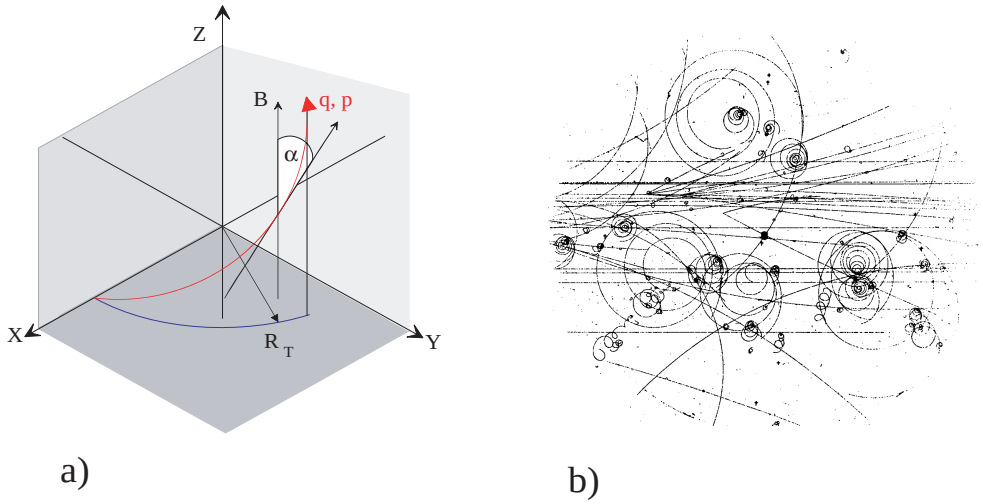

Figure 14: a) A particle with charge q and momentum p in a uniform magnetic field $\vec{B}$. b) Production of particle jets by 16 GeV negative pions in the first CERN liquid hydrogen bubble chamber. It was only 30 cm in diameter. CERN photo-ex/11465.

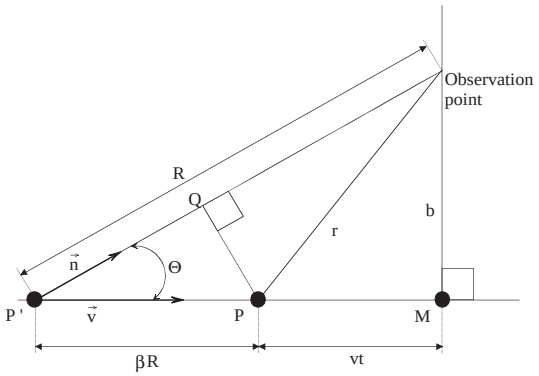

Figure 15: Present and retarded position of a charge in uniform motion. [2]

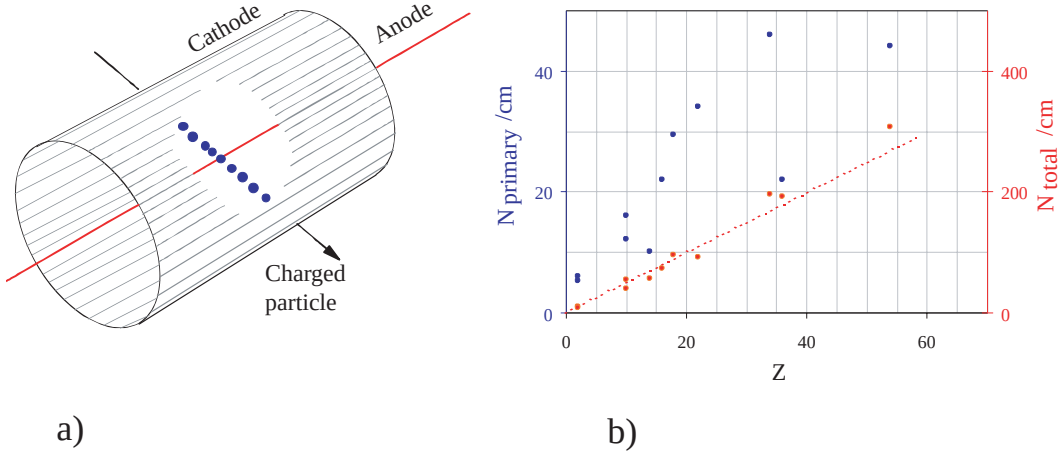

Figure 16: a) Straw tube design for charged particle detection. b) Primary and secondary ion pair production per unit length for gases at atmospheric pressure and for minimum ionising particles [11].

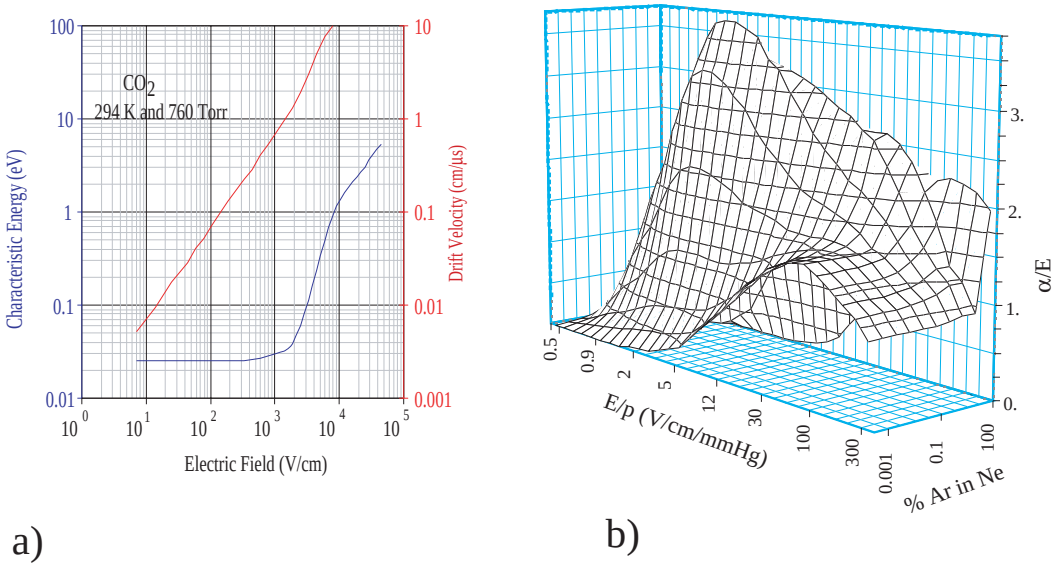

Figure 17: a) Characteristic energy and drift velocity of electrons in CO_2 as function of the electric field [11]. b) The first Townsend coefficient, α, as function of the electric field in a gas mixture of Ne and Ar [12].

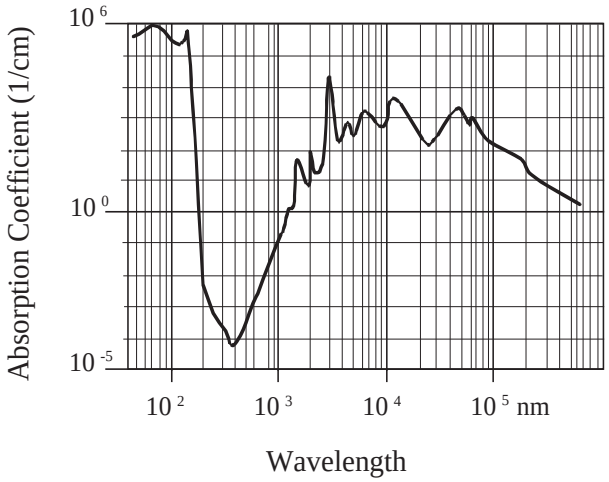

Figure 18: Absorption coefficient for water as function of wavelength. Energy can be stored in molecules as translational, rotational and vibrational energy. Translation can occur in the x, y or z direction. Rotation can occur around the x, y or z axis, except for linear molecules which only have two axes or rotation. Vibrations involve movements of the atoms of a molecule which produce no net translation or rotation. These various movements are a result of the combination of the normal modes of vibration. For a triatomic molecule these normal modes are symmetric, asymmetric and bending vibrations. In symmetric vibration, the two bonds shorten and lengthen together. In asymmetric vibration, one bond shortens while the other lengthens. In bending vibration, it is the bond angle that oscillates. From: `http://www4.ncsu.edu:8030/ ajschult/pchem/water/water.html`

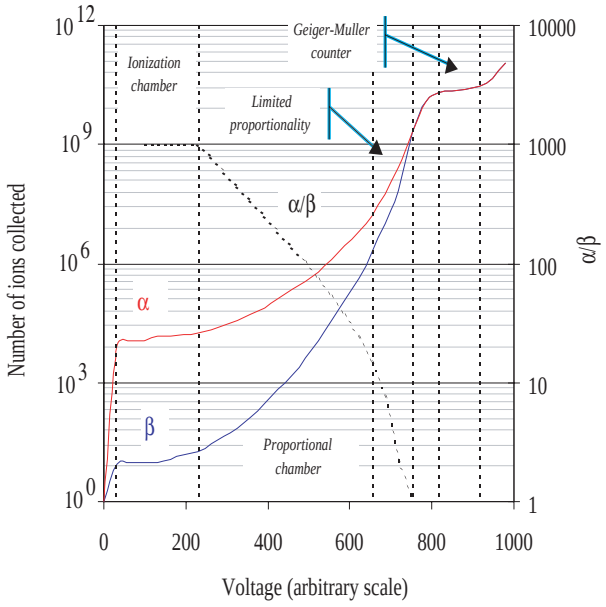

Figure 19: Gain and voltage characteristics for α and β particles in a proportional counter [11].

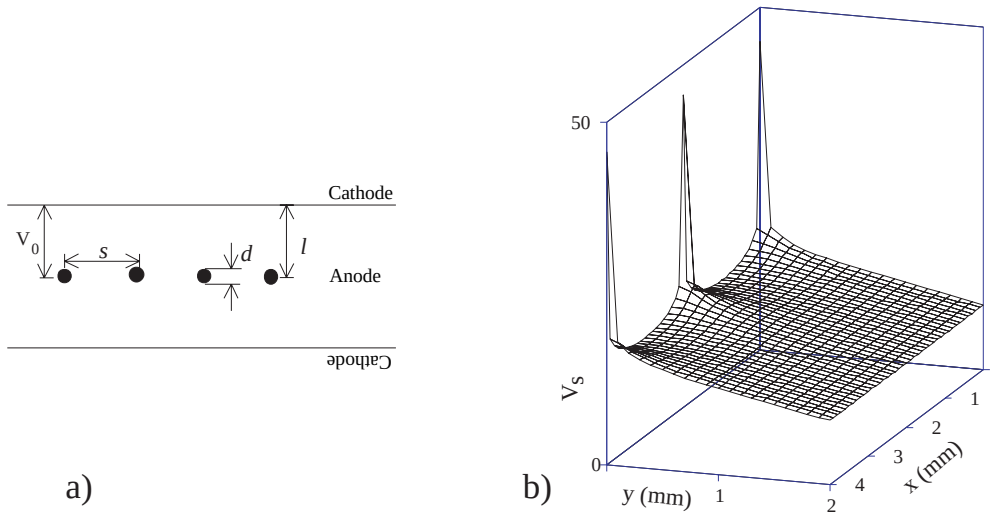

Figure 20: a) shows a schematic layout of a multiwire proportional chamber. b) is the calculated voltage for $l = 5$ mm, $s = 2$ mm and $d = 20\mu$m.

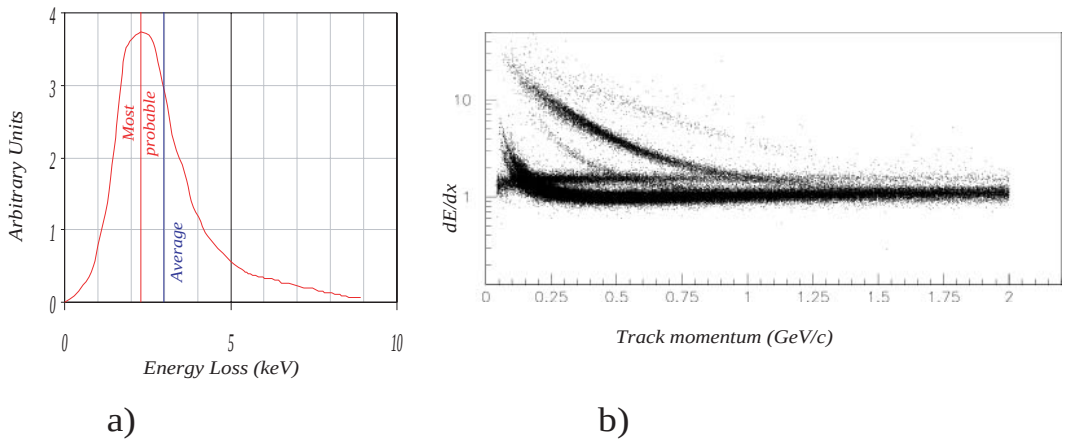

Figure 21: a) Ionisation energy loss for 3 GeV/c π in Ar/CH_4. Also indicated is the average and the most probable energy loss. b) Results from the DELPHI experiment at LEP. Notice the clear electron band and the proton and deuterium bands which are well populated at low momenta.

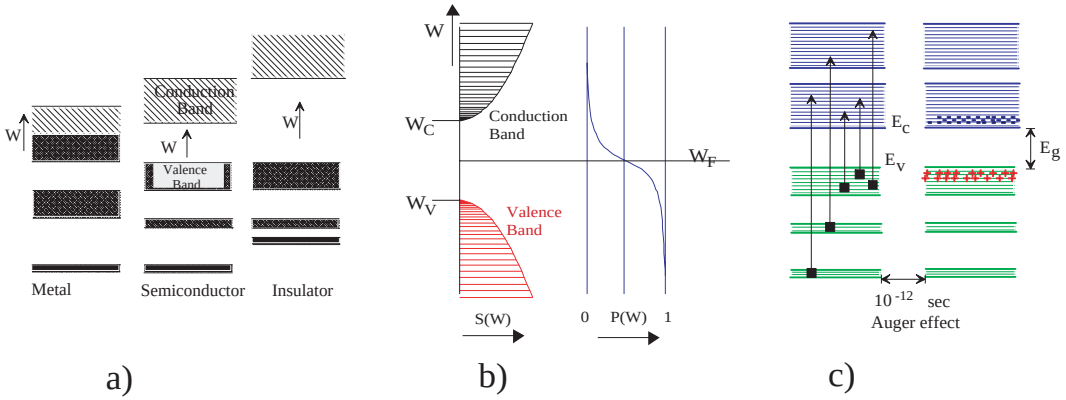

Figure 22: a) Allowed and forbidden bands. In a metal one band is only partially filled. The valence band is (nearly) full in a semiconductor and the conduction band is (nearly) empty. The energy gap is larger between the valence band and the conduction band in an insulator than in a semiconductor. b) The number of states, $S(W)$, and the probability that the states are occupied, $P(W)$, in a semiconductor. c) Excitation of electrons in a semiconductor due to the passage of a charged particle.

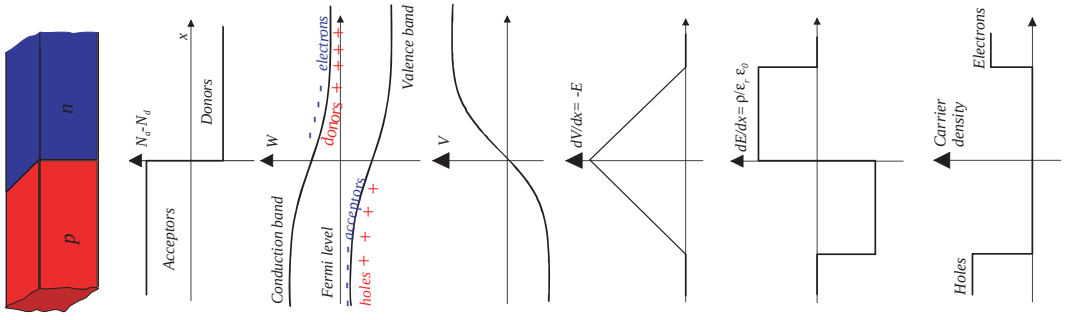

Figure 23: A p-n junction without bias. Note the peak electric field at the boundary between the p and the n. Also note the clear depletion layer shown in the last sketch. [16].

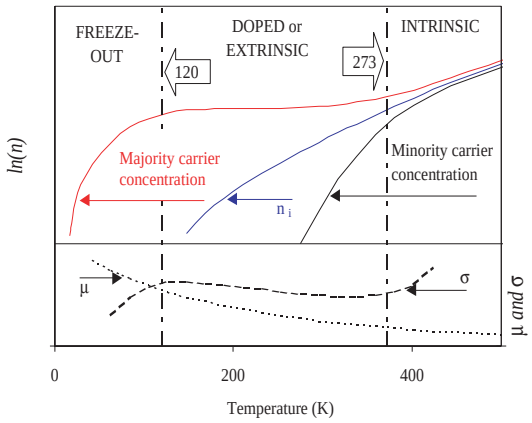

Figure 24: The variation with temperature of majority and minority carrier concentration, mobility μ and conductivity σ for a semiconductor.

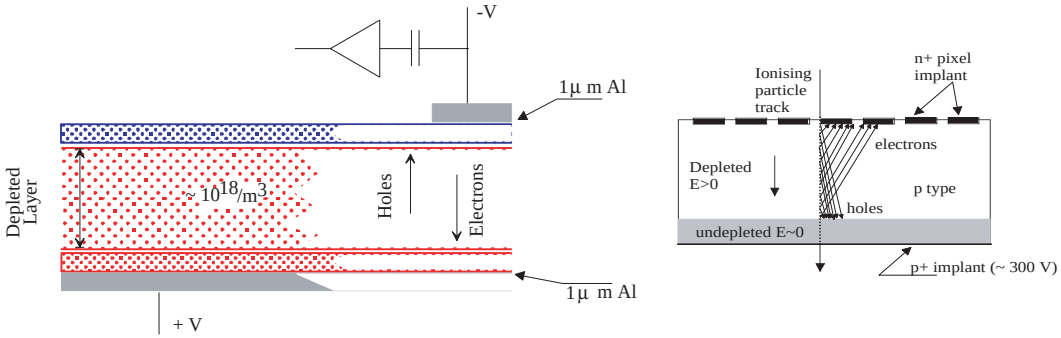

Figure 25: Sketch of possible configurations for a silicon detector.

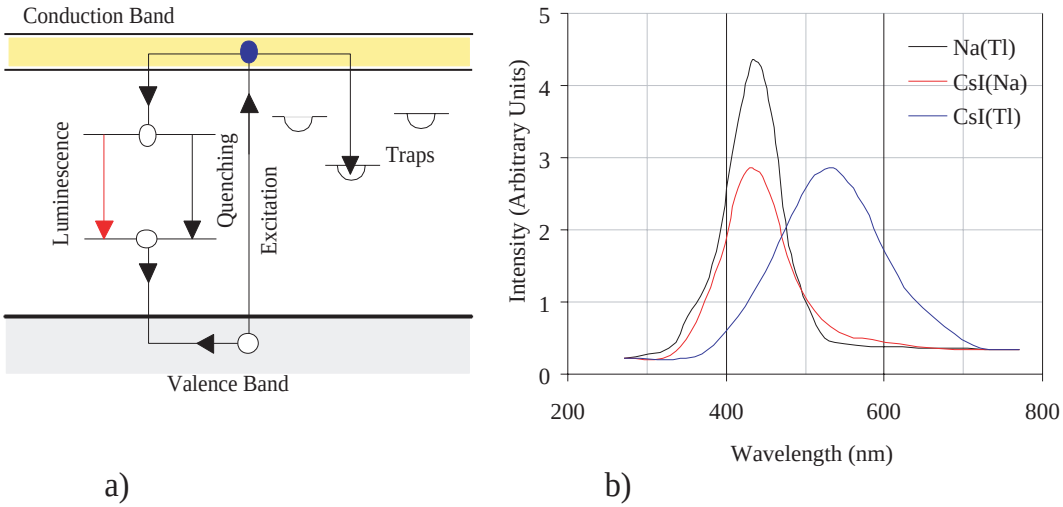

Figure 26: a) shows the band structure of an inorganic crystalline scintillator. b) scintillation intensity as function of wavelength.

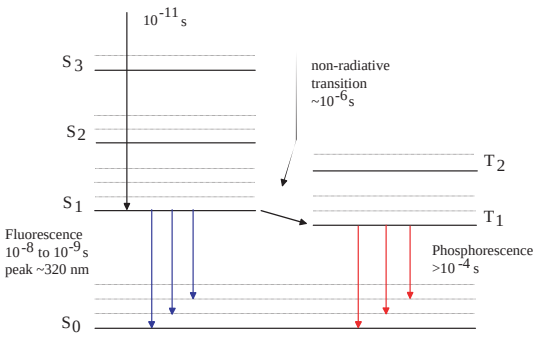

Figure 27: The energy level for the p-electrons in benzene, indicating the fast fluorescence and the retarded phosphorescence.

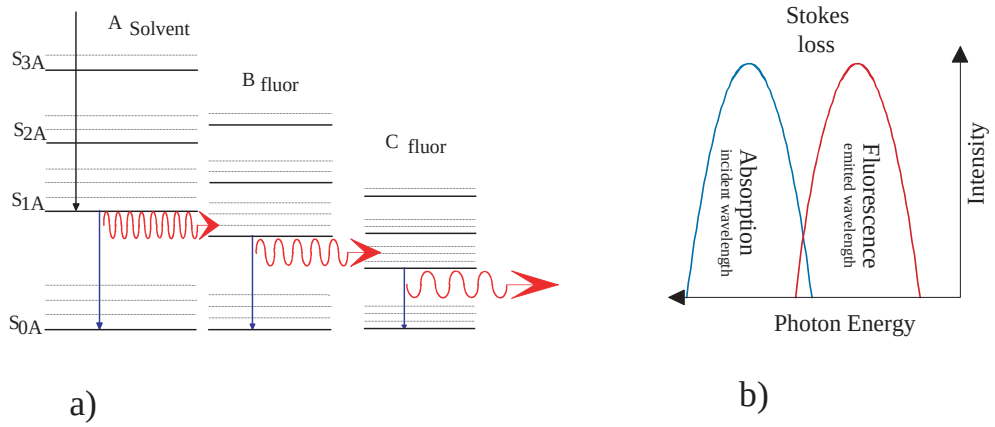

Figure 28: a) shows the wavelength shifting in an organic scintillator. b) The emitted wavelength is always longer or equal to the incident wavelength. The difference is absorbed as heat in the atomic lattice of the material.

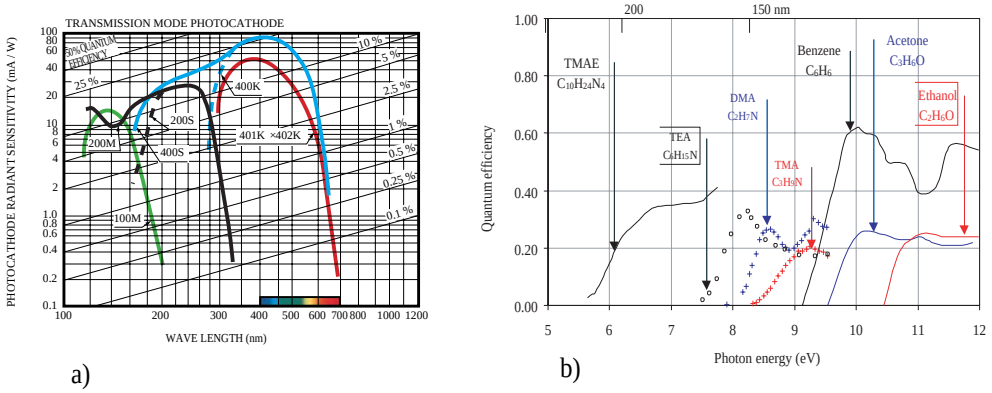

Figure 29: a) Quantum efficiency as function of wavelength for semitransparent photocathodes. Plot from `http://www.hamamatsu.com/` . b) Quantum efficiency as function of the photon energy for some photo sensitive vapours. Replotted from [21].

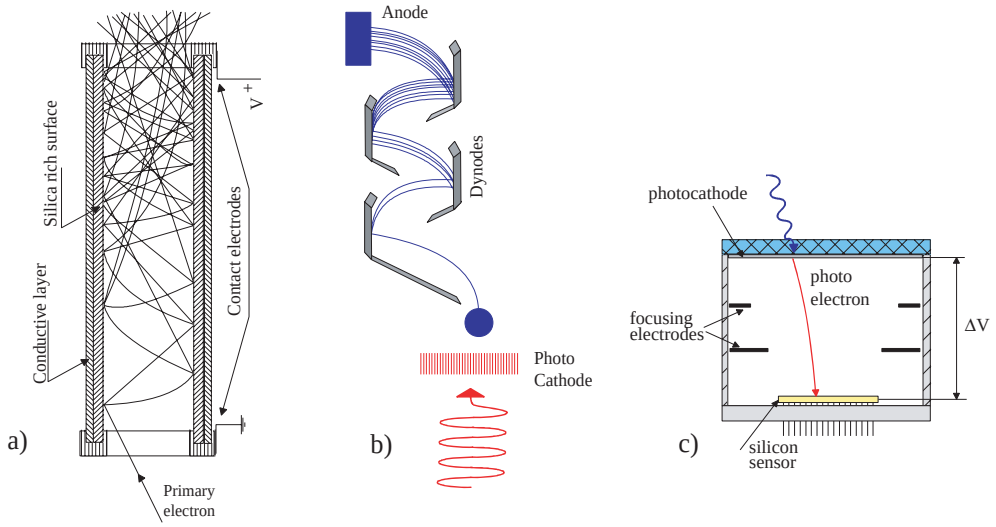

Figure 30: a) Operation of a single microchannel. Photocathode not shown. b) Photoelectron multiplier tube with photocathode and dynodes of secondary-electron emitting material. c) Is a sketch of a hybrid photo diode.

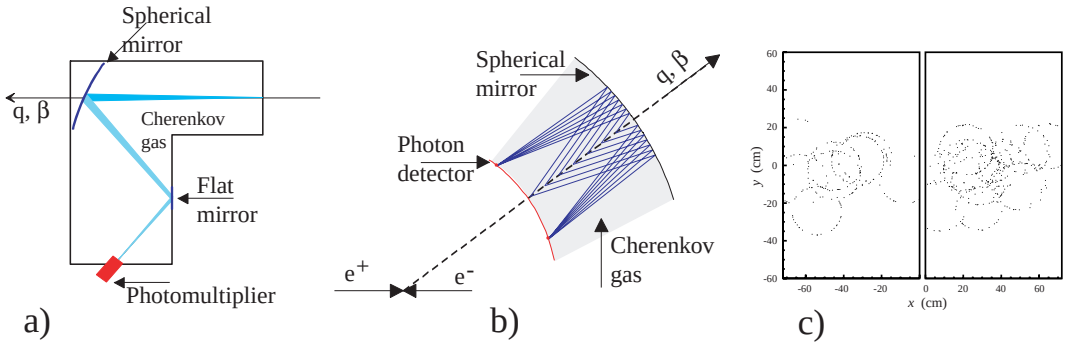

Figure 31: A threshold Cherenkov detector is outlined in a). b) shows a sketch of the principles of operation of a ring imaging Cherenkov detector. c) is an event display of a simulated event including a $B_d^0 \to \pi^+\pi^-$ event on the photodetector plane of a ring imaging Cherenkov detector. The detected photons are indicated by dots [24].

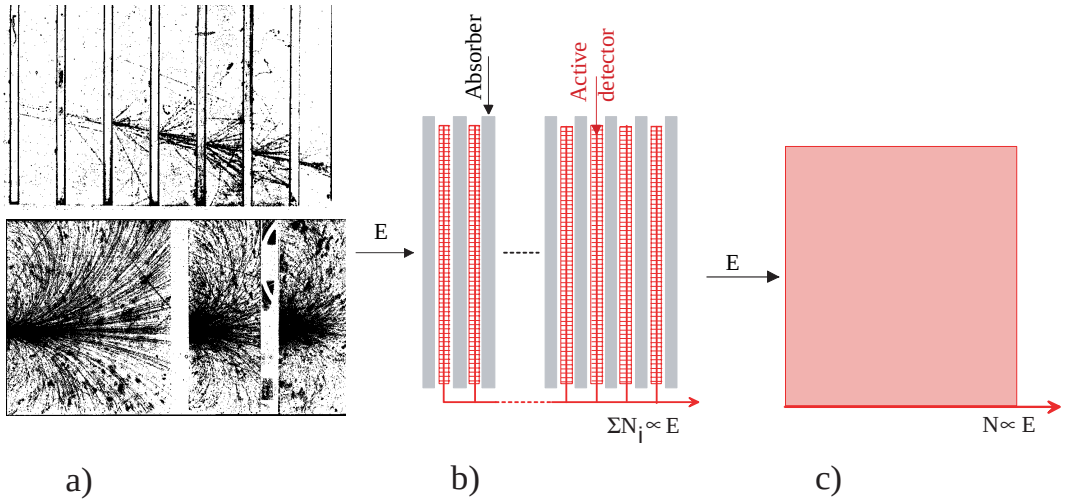

Figure 32: a) is a cloud chamber illustration [28] of the longitudinal and the lateral development of an electromagnetic shower in lead. In the top picture, the shower is initiated by an electron. Note that the electrons which emerge from the lead plates at large angles to the shower axis do not penetrate the following plate. These are low energy secondary electrons. This becomes clear in the bottom picture where the electrons, or positrons, are spread out with a magnetic field of 7500 gauss. b) and c) shows the working principle of a sampling and a homogenous calorimeter.

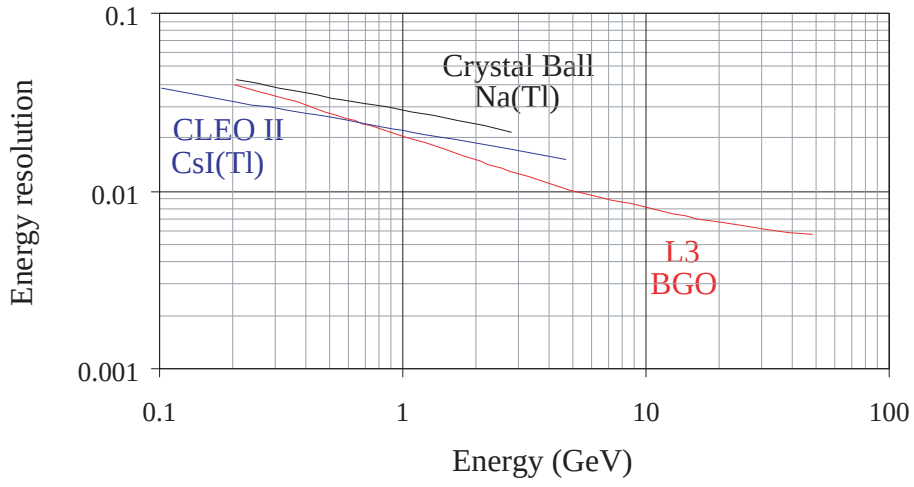

Figure 33: Energy resolution as function of energy for large detector systems. Replotted from [32].